

Discontinuous Galerkin method for computing gravitational waveforms from extreme mass ratio binaries

Scott E. Field^{1,*}, Jan S. Hesthaven^{2,†}, and Stephen R. Lau^{2,3,‡}

¹*Department of Physics, Brown University, Providence, RI 02912*

²*Division of Applied Mathematics, Brown University, Providence, RI 02912*

³*Mathematics and Statistics, University of New Mexico, Albuquerque, NM 87131*

Gravitational wave emission from extreme mass ratio binaries (EMRBs) should be detectable by the joint NASA–ESA LISA project, spurring interest in analytical and numerical methods for investigating EMRBs. We describe a discontinuous Galerkin (dG) method for solving the distributionally forced 1+1 wave equations which arise when modeling EMRBs via the perturbation theory of Schwarzschild blackholes. Despite the presence of jump discontinuities in the relevant polar and axial gravitational “master functions”, our dG method achieves global spectral accuracy, provided that we know the instantaneous position, velocity, and acceleration of the small particle. Here these variables are known, since we assume that the particle follows a timelike geodesic of the Schwarzschild geometry. We document the results of several numerical experiments testing our method, and in our concluding section discuss the possible inclusion of gravitational self–force effects.

PACS numbers: 04.25.Dm (Numerical Relativity), 02.70.Hm (Spectral Methods), 02.70.Jn (Collocation methods); AMS numbers: 65M70 (Spectral, collocation and related methods), 83-08 (Relativity and gravitational theory, Computational methods), 83C57 (General relativity, Black holes).

I. INTRODUCTION

An extreme mass ratio binary (EMRB) is a system comprised of small mass- m_p “particle” (possibly a main sequence star, neutron star, or stellar mass blackhole) orbiting a large mass- M blackhole, where the mass ratio $\mu = m_p/M \ll 1$. EMRB systems are expected to emit gravitational radiation in a low frequency band (10^{-5} to 10^{-1} Hz), and therefore offer the promise of detection by the joint NASA–ESA LISA project [1, 2]. A standard method for studying some EMRBs uses the perturbation theory of Schwarzschild blackholes in an approximation which treats the particle as point-like and responsible for generating small metric perturbations which radiate away to infinity. These perturbations influence the trajectory of particle, resulting in deviation from geodesic motion. Nevertheless, as a first and useful approximation, one may compute the emitted gravitational radiation, assuming that the particle worldline is a timelike geodesic in the Schwarzschild spacetime. More sophisticated approaches have included the effect of radiation reaction on the particle, usually through incorporation of a self–force (see Ref. [3] for a review) or a suitable approximation thereof [4]. Save for comments in the conclusion, this paper ignores self–force, although our methods may prove useful when it is included.

A chief goal of gravitational wave signal analysis is to determine the spacetime structure of a given binary system from its experimentally measured waveform [2, 5], a goal likely facilitated by numerical simulation. For the scenario we consider, simulation of EMRBs entails numerical evolution of Schwarzschild perturbations. The theory of such perturbations is well studied, and starts with pioneering investigations by Regge and Wheeler [6] and by Zerilli [7]. A detailed presentation of the subject is beyond the scope of our paper, and we point the reader to Refs. [8, 9] for modern accounts of the subject which supply the necessary background and references for our

* Scott.Field@brown.edu, [†] Jan.Hesthaven@brown.edu, [‡] srlau@math.unm.edu

work. Nevertheless, in order to provide some context, we now give a brief overview. We consider a small perturbation $\delta g_{\mu\nu}$ of the background Schwarzschild metric $g_{\mu\nu}$ given in (4), where the perturbation satisfies the linearized Einstein equation. In our scenario the stress–energy tensor $T_{\mu\nu}$ given in (C14) corresponds to a material point particle, and is therefore a distribution. The metric perturbation $\delta g_{\mu\nu}$ is clearly tensorial; nevertheless, the perturbations can be reconstructed from a collection of scalar *master functions*. Remarkably, the master functions are governed by forced scalar wave equations with the following form:¹

$$-\partial_t^2 \Psi_{\ell m} + \partial_x^2 \Psi_{\ell m} - V_\ell(r) \Psi_{\ell m} = f(r) [G_{\ell m}(t, r) \delta(r - r_p(t)) + F_{\ell m}(t, r) \delta'(r - r_p(t))]. \quad (1)$$

The coordinates here are the areal radius r , the Regge–Wheeler tortoise coordinate [10] $x = r + 2M \log(\frac{1}{2}r/M - 1)$, and the time–dependent radial location $r_p(t)$ of the particle. Furthermore, $V_\ell(r)$ is a potential, and $\Psi_{\ell m}(t, r)$ is one of the master functions. Since master functions arise in a (tensor) spherical harmonic decomposition of the perturbative equations for $\delta g_{\mu\nu}$, they carry multipole indices (ℓ, m) , where $\ell \geq 2$, $|m| \leq \ell$. The *distributional* inhomogeneity on the right–hand side of (1) stems from $T_{\mu\nu}$, and it involves Dirac delta functions, as well as the ordinary functions $F_{\ell m}(t, r)$, $G_{\ell m}(t, r)$, and $f(r) = 1 - 2M/r$. Perturbations of the Schwarzschild metric are characterized as either *polar* or *axial*, and each case corresponds to particular functions. The polar case corresponds to the Zerilli potential [7]

$$V_\ell^Z(r) = \frac{2f(r)}{(n_\ell r + 3M)^2} \left[n_\ell^2 \left(1 + n_\ell + \frac{3M}{r} \right) + \frac{9M^2}{r^2} \left(n_\ell + \frac{M}{r} \right) \right], \quad (2)$$

where $n_\ell = (\ell + 2)(\ell - 1)/2$, and the Zerilli–Moncrief master function Ψ^{ZM} . Appendix C provides explicit formulas for $F_{\ell m}^{\text{ZM}}(t, r)$ and $G_{\ell m}^{\text{ZM}}(t, r)$. The axial case corresponds to the Regge–Wheeler potential [6]

$$V_\ell^{\text{RW}}(r) = \frac{f(r)}{r^2} \left[\ell(\ell + 1) - \frac{6M}{r} \right], \quad (3)$$

and for this case we choose to work with the Cunningham–Price–Moncrief master function Ψ^{CPM} [9]. Appendix C also gives explicit formulas for $F_{\ell m}^{\text{CPM}}(t, r)$ and $G_{\ell m}^{\text{CPM}}(t, r)$.

A number of numerical methods for solving (1) as an initial boundary value problem, and therefore modeling EMRBs in the time–domain, have appeared in the literature. In particular, we note Lousto’s fourth–order algorithm [11] based on spacetime integration of (1) and careful Taylor series arguments, and Sopena and Laguna’s adaptive finite–element approach [9]. Jung, Khanna, and Nagle have applied a spectral collocation method to the perturbation equations for head–on collisions, using spectral filtering to handle the delta function terms [12]. Most recently, Canizares and Sopena have proposed a multidomain spectral collocation method, with the particle location chosen between spectral elements [13]. Clearly, the key difficulty to overcome is the distributional forcing; however, the problem should be amenable to a high–order accurate method, since —apart from possible transients— the solutions we seek to compute are everywhere smooth, except for jump discontinuities at the particle location. As a suitable high–order scheme for solving (1), we propose a discontinuous Galerkin (dG) method, and our approach shares some similarities

¹ We could instead work with the equation

$$-\partial_t^2 \Psi_{\ell m} + \partial_x^2 \Psi_{\ell m} - V_\ell(r) \Psi_{\ell m} = \mathcal{G}_{\ell m}(t) \delta(r - r_p(t)) + \mathcal{F}_{\ell m}(t) \delta'(r - r_p(t)),$$

where $\mathcal{G}_{\ell m}(t)$ and $\mathcal{F}_{\ell m}(t)$ depend only on t , and not on r . The relationships between $\mathcal{G}_{\ell m}(t)$ and $\mathcal{F}_{\ell m}(t)$ and our $G_{\ell m}(t, r)$ and $F_{\ell m}(t, r)$ follows from comparison between the right–hand sides of Eq. (A1) and the last equation.

with Refs. [9, 12, 13], in particular we also ensure that the particle always lies at the interface between domain intervals. DG methods are widely used for wave-dominated problems, such as electromagnetic scattering [14, 15], and in nonlinear fluid dynamics [15]. Our work is one of the first applications of dG methods to the modeling of gravitational waves (see also [16]), and the first dG computation of gravitational metric perturbations driven by a point-particle. Improving upon low-order methods, our method achieves global spectral accuracy (see also Refs. [12, 13]).

This paper is organized as follows. Section II provides further background necessary to understand the physical model. In particular, this section discusses the particle motion, the resulting jump conditions in the master functions, and a coordinate transformation adapted to the particle history. This background allows us to rewrite (1) as a first-order system which features only *undifferentiated* delta-functions in the forcing. Section III describes our dG scheme as applied to the first-order system obtained in the previous section. Here we focus not only on the local representation of the solutions, but also on how delta function terms are incorporated into the numerical flux function. Section IV documents the results of several experiments testing our method, and it compares our results with others found in the existing literature. In the concluding section, we discuss, in particular, the possible inclusion of radiation reaction. Several appendices collect technical results not given in the main part of the paper.

II. PRELIMINARIES

Throughout, we use both ∂ and subscript notation for partial differentiation. For example, $\partial_r \Psi$ and Ψ_r are the same. We use an over-dot to denote $\partial/\partial t$ differentiation, and sometimes a prime for differentiation by argument. The labels ($\ell, m, \text{CPM/ZM}$) are suppressed throughout.

A. Particle motion

In standard coordinates, the Schwarzschild line-element reads

$$ds^2 = -f dt^2 + f^{-1} dr^2 + r^2 (d\theta^2 + \sin^2 \theta d\phi^2), \quad (4)$$

where t labels the preferred static-time slices and, as mentioned, r is areal radius. Owing to the spherical symmetry of the line-element, we may assume, without loss of generality, that the particle trajectory $(r_p(t), \theta_p(t), \phi_p(t)) = (r_p(t), \pi/2, \phi_p(t))$ lies in the equatorial plane [17]. Introducing the *eccentricity* constant e , *semi-latus rectum* constant p , and the parameterization $r_p(t) = pM/(1 + e \cos \chi(t))$, we obtain the particle trajectory $(r_p(t), \phi_p(t))$ by integration of the following system which describes timelike geodesic motion: [9, 17, 18, 19]

$$\frac{d\phi}{dt} = \frac{(p - 2 - 2e \cos \chi)(1 + e \cos \chi)^2}{Mp^{3/2} [(p - 2)^2 - 4e^2]^{1/2}} \quad (5a)$$

$$\frac{d\chi}{dt} = \frac{(p - 2 - 2e \cos \chi)(1 + e \cos \chi)^2 [p - 6 - 2e \cos \chi]^{1/2}}{Mp^2 [(p - 2)^2 - 4e^2]^{1/2}}. \quad (5b)$$

We use $\chi(t)$ rather than $r_p(t)$, since the former increases monotonically through radial turning points. In our scenario, integration of the system (5) is independent of (1). Therefore, we may view the particle path, and so the right-hand side of (1), as predetermined. We shall be interested in the parameter restriction $0 \leq e < 1$, for which the motion occurs between two turning points and the orbit is bounded. The periastron and apastron occur respectively at $pM/(1 + e)$ and

$pM/(1-e)$, and for $e = 0$ the orbit is circular. Measured in coordinate time t , an eccentric orbit executes a radial period in time T_r given by [19]

$$T_r = C \int_0^{2\pi} d\chi (1 + e \cos \chi)^{-2} \left[1 - \frac{2(3 + e \cos \chi)}{p} \right]^{-1/2} \left[1 - \frac{2(1 + e \cos \chi)}{p} \right]^{-1} \quad (6)$$

$$C = p^{3/2} M \left[\left(1 - \frac{2}{p} \right)^2 - \left(\frac{2e}{p} \right)^2 \right]^{1/2}.$$

When $e \neq 0$, we average physical quantities over 4 radial periods, as defined by Eq. (66).

B. Jump conditions

The forcing (1) induces jump conditions on the master function. Derived in Appendix A, these are the following:

$$(f_p^2(t) - \dot{r}_p^2(t)) [[\Psi]] = f_p(t) F(t, r_p(t)) \quad (7a)$$

$$\begin{aligned} 2\dot{r}_p(t) \partial_t [[\Psi]] + (\ddot{r}_p(t) - f_p(t) g_p(t)) [[\Psi]] + (f_p^2(t) - \dot{r}_p^2(t)) [[\Psi_r]] \\ = f_p(t) G(t, r_p(t)) - g_p(t) F(t, r_p(t)) - f_p(t) F_r(t, r_p(t)), \end{aligned} \quad (7b)$$

where the subscript r in $F_r(t, r)$ denotes partial differentiation with respect to the second slot, and

$$f_p(t) = f(r_p(t)), \quad g_p(t) = f'(r_p(t)) \neq \partial_t f_p(t) \quad (8)$$

are shorthands. In (7) our notation for a time-dependent jump is, for example,

$$[[\Psi]](t) \equiv \lim_{\epsilon \rightarrow 0^+} [\Psi(t, r_p(t) + \epsilon) - \Psi(t, r_p(t) - \epsilon)]. \quad (9)$$

Defining the particle velocity as $v_p(t) = \dot{x}_p(t) = \dot{r}_p(t)/f_p(t)$, we see that (7a) has the form

$$f_p(t)(1 - v_p^2(t)) [[\Psi]] = F(t, r_p(t)), \quad (10)$$

confirming that the jump $[[\Psi]]$ is well-defined for a subluminal particle speed, $|v_p| < 1$. Therefore, we may safely make the substitution

$$[[\Psi]] = \frac{f_p(t) F(t, r_p(t))}{f_p^2(t) - \dot{r}_p^2(t)} \quad (11)$$

in all formulas which follow. Differentiation of (11) gives

$$\begin{aligned} \partial_t [[\Psi]] = \frac{2f_p(t) \dot{r}_p(t) F(t, r_p(t)) [\ddot{r}_p(t) - f_p(t) g_p(t)]}{(f_p^2(t) - \dot{r}_p^2(t))^2} \\ + \frac{g_p(t) \dot{r}_p(t) F(t, r_p(t)) + f_p(t) F_t(t, r_p(t)) + f_p(t) \dot{r}_p(t) F_r(t, r_p(t))}{f_p^2(t) - \dot{r}_p^2(t)}. \end{aligned} \quad (12)$$

Finally, we may express (7b) as

$$\begin{aligned} [[\Psi_r]] = [-2\dot{r}_p(t) \partial_t [[\Psi]] - (\ddot{r}_p(t) - f_p(t) g_p(t)) [[\Psi]] \\ + f_p(t) G(t, r_p(t)) - g_p(t) F(t, r_p(t)) - f_p(t) F_r(t, r_p(t))] / (f_p^2(t) - \dot{r}_p^2(t)), \end{aligned} \quad (13)$$

with the understanding that here $[[\Psi]]$ and $\partial_t [[\Psi]]$ respectively stand for (11) and (12). Again note that $f_p^2(t) - \dot{r}_p^2(t) > 1$ for a subluminal particle speed, whence the jumps $\partial_t [[\Psi]]$ and $[[\Psi_r]]$ given by Eqs. (12) and (13) are finite. The formulas

$$[[\Psi_t]] = \partial_t [[\Psi]] - \dot{r}_p(t) [[\Psi_r]], \quad [[\Psi_x]] = f_p(t) [[\Psi_r]] \quad (14)$$

prove useful later.

C. Coordinate transformation adapted to particle history

Now assume that $x \in [a, b]$ specifies the computational domain and the time-dependent particle location $x_p = x_p(t)$ obeys $a < x_p(t) < b$, $\forall t$. We enact the coordinate transformation

$$t = \lambda \quad (15)$$

$$x = a + \frac{x_p - a}{\xi_p - a}(\xi - a) + \frac{(b - x_p)(\xi_p - a) - (x_p - a)(b - \xi_p)}{(\xi_p - a)(b - \xi_p)(b - a)}(\xi - a)(\xi - \xi_p), \quad (16)$$

with the understanding that $x_p = x_p(\lambda)$ is explicitly time-dependent. The transformation obeys the following criteria: (i) t and λ label the same time slices; (ii) $x(\lambda, \xi_p) = x_p(\lambda)$, with $\xi_p = \text{constant}$ and $a < \xi_p < b$; (iii) $x(\lambda, a) = a$ and $x(\lambda, b) = b$. We further require (iv) that the transformation is invertible on $[a, b]$. This will only hold provided the point

$$\xi_{\text{critical}} = \frac{(\xi_p + a)(\xi_p - x_p(\lambda)) + (x_p(\lambda) - a)(b - \xi_p)}{(\xi_p - x_p(\lambda))} \quad (17)$$

lies outside of the interval $[a, b]$. This is not a restriction of our method *per se*, and a coordinate transformation satisfying conditions (i) through (iv) may always be found. We have chosen to work with this one only for its simplicity.

Differentiations of (16) yield

$$\frac{\partial x}{\partial \lambda} = \frac{(\xi - a)(b - \xi)x'_p(\lambda)}{(\xi_p - a)(b - \xi_p)} \quad (18)$$

$$\frac{\partial x}{\partial \xi} = \frac{(2\xi - \xi_p - a)(\xi_p - x_p(\lambda)) + (x_p(\lambda) - a)(b - \xi_p)}{(\xi_p - a)(b - \xi_p)} \quad (19)$$

$$\frac{\partial^2 x}{\partial \xi^2} = \frac{2(\xi_p - x_p(\lambda))}{(\xi_p - a)(b - \xi_p)}, \quad (20)$$

and these expressions appear in later formulas.

Under the coordinate transformation, the line-element (4) acquires a shift vector,

$$ds^2 = -N^2 d\lambda^2 + L^2 (d\xi + \beta^\xi d\lambda)^2 + r^2 (d\theta^2 + \sin^2 \theta d\phi^2). \quad (21)$$

Here $N = f^{1/2}$, $L = f^{1/2} \partial x / \partial \xi$, with f understood as $f(r(x(\lambda, \xi)))$. The shift vector is

$$\beta^\xi = \frac{\partial x / \partial \lambda}{\partial x / \partial \xi} = \frac{(\xi - a)(b - \xi)x'_p(\lambda)}{(2\xi - \xi_p - a)(\xi_p - x_p(\lambda)) + (x_p(\lambda) - a)(b - \xi_p)}, \quad (22)$$

and we will also need

$$\frac{\partial \beta^\xi}{\partial \xi} = \frac{(A\xi^2 + B\xi + C)x'_p(\lambda)}{[(2\xi - \xi_p - a)(\xi_p - x_p(\lambda)) + (x_p(\lambda) - a)(b - \xi_p)]^2}, \quad (23)$$

where $A = 2(x_p(\lambda) - \xi_p)$, $B = 2(ab + \xi_p^2 - (a+b)x_p(\lambda))$, and $C = (a^2 + b^2)x_p(\lambda) - a(b - \xi_p)^2 - b(a^2 + \xi_p^2)$. The velocity variable $v = L\beta^\xi / N = \partial x / \partial \lambda$ obeys

$$v(\lambda, a) = 0, \quad v(\lambda, \xi_p) = x'_p(\lambda), \quad v(\lambda, b) = 0. \quad (24)$$

Since $|x'_p(\lambda)| < 1$, we have $|v(\lambda, \xi)| < 1$ uniformly in ξ , assuming appropriately chosen ξ_p , a , and b . The vector field $\partial / \partial \lambda$ is not the Killing direction, and it does not point orthogonal to the constant- λ slices. To relate the $\partial / \partial \lambda$ direction to the unit-normal² u of the slicing, first consider

² Here we use coordinate-free abstract notation for the *vector fields* u , \bar{u} , and n .

$g_{\lambda\lambda} = -N^2 + L^2(\beta^\xi)^2 = -N^2(1 - v^2) = -(N/\gamma)^2$, where $\gamma = (1 - v^2)^{-1/2}$ is the relativistic factor. Therefore, the vector field

$$\bar{u} = \gamma N^{-1} \partial / \partial \lambda \quad (25)$$

is normalized, and one of its integral curves is the particle history. From standard formulas

$$N^{-1}(\partial / \partial \lambda - \beta^\xi \partial / \partial \xi) = \gamma^{-1} \bar{u} - v L^{-1} \partial / \partial \xi, \quad (26)$$

so that $\bar{u} = \gamma u + v \gamma n$. Here $g(n, n) = L^{-2} g_{\xi\xi} = 1$, whence $n = L^{-1} \partial / \partial \xi$ is a normalized spacelike vector field. These formulas show that the spacetime dependent parameter v determines a local boost in the tangent space of each spacetime point in the coordinate domain. At $\xi = \xi_p$ this boost relates the slice normal u to the particle direction.

D. Wave equation as a first-order system in (λ, ξ)

Retaining the same letter Ψ to denote the wave field $\Psi(\lambda, r(x(\lambda, \xi)))$ in the new coordinates, we introduce the gradient $\Phi = \partial_\xi \Psi$. Notice that $\partial_x \Psi = f \partial_r \Psi$ in the old system corresponds to $(\partial x / \partial \xi)^{-1} \Phi$ in the new system. The following first-order system in the (λ, ξ) coordinates corresponds to the original second-order wave equation (1):

$$\partial_\lambda \Psi = \beta^\xi \Phi - \Pi \quad (27a)$$

$$\partial_\lambda \Pi = \beta^\xi \partial_\xi \Pi - (\partial x / \partial \xi)^{-1} \partial_\xi [(\partial x / \partial \xi)^{-1} \Phi] + V(r) \Psi + J_1 \delta(\xi - \xi_p) \quad (27b)$$

$$\partial_\lambda \Phi = \partial_\xi (\beta^\xi \Phi) - \partial_\xi \Pi + J_2 \delta(\xi - \xi_p), \quad (27c)$$

where Eq. (27a) defines the variable Π . The λ -dependent functions

$$J_1 = -\beta^\xi [[\Pi]] + (\partial x / \partial \xi)^{-2} [[\Phi]], \quad J_2 = -\beta^\xi [[\Phi]] + [[\Pi]]. \quad (28)$$

implement the jump conditions collected in Section II B, where in terms of (14)

$$[[\Pi]] = -[[\Psi_t]], \quad [[\Phi]] = (\partial x / \partial \xi) [[\Psi_x]]. \quad (29)$$

The jumps (28) can be recovered by integrating (27) against a test function over the region $(\xi_p - \epsilon, \xi_p + \epsilon)$, performing an integration by parts, and taking the $\epsilon \rightarrow 0^+$ limit. Smooth terms vanish in the limit. Thus, the system (27), with this choice of J_1 and J_2 , is the first order form of (1) by construction.

III. DISCONTINUOUS GALERKIN METHOD

Following Ref. [15], this section describes the nodal discontinuous Galerkin (dG) method used to numerically solve (27). Ultimately, we adopt a method-of-lines strategy, and here describe the relevant semi-discrete scheme which arises upon spatial approximation of (27) by the dG method. In all numerical experiments considered later, we have carried out the temporal integration with an explicit fourth-order Runge-Kutta method, either one of low-storage [20] or the classical one. DG methods incorporate and build upon finite-element (FE), finite-volume (FV), and spectral methods, and in this section the reader will recognize the features our dG approach shares with these more traditional methods. For example, on each subdomain our approach features a weak formulation of Legendre collocation, and our technique for coupling subdomains draws on FV methods.

A. Local approximation of the system (27)

Our computational domain Ω is the closed ξ -interval $[a, b]$. We cover Ω with $K > 1$ non-overlapping intervals $D^k = [a^k, b^k]$, where $a = a^1$, $b = b^K$, and $b^{k-1} = a^k$ for $k = 2, \dots, K$. We further assume that the particle location $\xi_p = b^{k_p} = a^{k_p+1}$ lies at the endpoint shared by D^{k_p} and D^{k_p+1} , with $1 \leq k_p < K$. On each interval D^k , we approximate each component of the system vector (Ψ, Π, Φ) by a local interpolating polynomial of degree N . For example,

$$\Psi_h^k(\lambda, \xi) = \sum_{j=0}^N \Psi(\lambda, \xi_j^k) \ell_j^k(\xi) \quad (30)$$

approximates Ψ , where $\ell_j^k(\xi)$ is the j th Lagrange polynomial belonging to D^k ,

$$\ell_j^k(\xi) = \prod_{\substack{i=0 \\ i \neq j}}^N \frac{\xi - \xi_i^k}{\xi_j^k - \xi_i^k}. \quad (31)$$

Evidently, the polynomial Ψ_h^k interpolates Ψ at the ξ_j^k . To define the nodes ξ_j^k , consider the mapping from the unit interval $[-1, 1]$ to D^k ,

$$\xi^k(u) = a^k + \frac{1}{2}(1+u)(b^k - a^k), \quad (32)$$

and the $N+1$ Legendre–Gauss–Lobatto (LGL) nodes u_j . The u_j are the roots of the equation

$$(1 - u^2)P'_N(u) = 0, \quad (33)$$

where $P_N(u)$ is the N th degree Legendre polynomial, and the physical nodes are simply $\xi_j^k = \xi^k(u_j)$. In vector notation the approximation (30) takes the form

$$\Psi_h^k(\lambda, \xi) = \Psi_h^k(\lambda)^T \ell^k(\xi), \quad (34)$$

in terms of the column vectors

$$\Psi_h^k(\lambda) = [\Psi(\lambda, \xi_0^k), \dots, \Psi(\lambda, \xi_N^k)]^T, \quad \ell^k(\xi) = [\ell_0^k(\xi), \dots, \ell_N^k(\xi)]^T. \quad (35)$$

We also need to approximate by polynomials various products, for example $(\partial x / \partial \xi) \Phi$. Such approximations are achieved through pointwise representations such as

$$(x_\xi \Phi)_h^k(\lambda, \xi) = \sum_{j=0}^N x_\xi(\lambda, \xi_j^k) \Phi(\lambda, \xi_j^k) \ell_j^k(\xi). \quad (36)$$

Here, and in what follows, we use the shorthands $x_\xi = \partial x / \partial \xi$ and $x_{\xi\xi} = \partial^2 x / \partial \xi^2$. Our vector notation for this example will be $(x_\xi \Phi)_h^k(\lambda, \xi) = (\mathbf{x}_\xi \Phi)_h^k(\lambda)^T \ell^k(\xi)$.

On each interval D^k and for each solution component, we define local residuals,

$$(R_\Psi)_h^k = \partial_\lambda \Psi_h^k - (\beta^\xi \Phi)_h^k + \Pi_h^k \quad (37a)$$

$$(R_\Pi)_h^k = \partial_\lambda \Pi_h^k - \partial_\xi (\beta^\xi \Pi)_h^k + (\Pi \partial_\xi \beta^\xi)_h^k + \partial_\xi (x_\xi^{-2} \Phi)_h^k + (x_\xi^{-3} x_{\xi\xi} \Phi)_h^k - (V \Psi)_h^k \quad (37b)$$

$$(R_\Phi)_h^k = \partial_\lambda \Phi_h^k - \partial_\xi (\beta^\xi \Phi)_h^k + \partial_\xi \Pi_h^k, \quad (37c)$$

measuring the extent to which our approximations satisfy the original system of PDE. We define these residuals on open intervals $(a^k, b^k) \subset D^k$, but have assumed that the particle location $\xi_p =$

$b^{k_p} = a^{k_p+1}$ lies at an endpoint. Therefore, in the residuals (37) we have not yet included the δ -function contributions appearing in (27).

To motivate our derivation of a numerical approximation to (27), we first consider the k th inner product

$$(u, v)_{D^k} \equiv \int_{a^k}^{b^k} d\xi u(\xi) v(\xi) \quad (38)$$

and the expressions $(\ell_j^k, (R_\Psi)_h^k)_{D^k}$, $(\ell_j^k, (R_\Pi)_h^k)_{D^k}$, and $(\ell_j^k, (R_\Phi)_h^k)_{D^k}$. Namely, the inner products between the residual components (37) and the j th Lagrange polynomial on D^k . We call the requirement that *all* these inner products $(\ell_j^k, (R_\Psi)_h^k)_{D^k}$, $(\ell_j^k, (R_\Pi)_h^k)_{D^k}$, $(\ell_j^k, (R_\Phi)_h^k)_{D^k}$ vanish $\forall j$ the k th *Galerkin conditions*. For now, we focus on the Φ equation as a representative example, but will later also consider the Ψ and Π equations.

Enforcement of the Galerkin conditions on each D^k will not recover a meaningful global solution, since they provide no mechanism for coupling of the individual local solutions on the different intervals. Notice that, upon integration by parts, we may express the inner product as follows:

$$\begin{aligned} (\ell_j^k, (R_\Phi)_h^k)_{D^k} &= \int_{a^k}^{b^k} d\xi [\ell_j^k(\xi) \partial_\lambda \Phi_h^k(\lambda, \xi) + \ell_j^{k'}(\xi) (\beta^\xi \Phi)_h^k(\lambda, \xi) - \ell_j^{k'}(\xi) \Pi_h^k(\lambda, \xi)] \\ &\quad - [(\beta^\xi \Phi)_h^k(\lambda, \xi) - \Pi_h^k(\lambda, \xi)] \ell_j^k(\xi) \Big|_{a^k}^{b^k}. \end{aligned} \quad (39)$$

Therefore, in lieu of (39) with $(\ell_j^k, (R_\Phi)_h^k)_{D^k} = 0$, we enforce the equation

$$\begin{aligned} 0 &= \int_{D^k} d\xi [\ell_j^k(\xi) \partial_\lambda \Phi_h^k(\lambda, \xi) + \ell_j^{k'}(\xi) (\beta^\xi \Phi)_h^k(\lambda, \xi) - \ell_j^{k'}(\xi) \Pi_h^k(\lambda, \xi)] \\ &\quad - [\beta^\xi(\lambda, \xi) (\Phi_h^k)^* - (\Pi_h^k)^*] \ell_j^k(\xi) \Big|_{a^k}^{b^k}. \end{aligned} \quad (40)$$

This equation features *numerical fluxes*, $-\beta^\xi(\lambda, a^k) (\Phi_h^k)^* + (\Pi_h^k)^*$ and $-\beta^\xi(\lambda, b^k) (\Phi_h^k)^* + (\Pi_h^k)^*$, rather than boundary fluxes, $-(\beta^\xi \Phi)_h^k(\lambda, a^k) + \Pi_h^k(\lambda, a^k)$ and $-(\beta^\xi \Phi)_h^k(\lambda, b^k) + \Pi_h^k(\lambda, b^k)$, thereby coupling adjacent subdomains. The numerical fluxes are determined by (as yet not chosen) functions

$$(\Pi_h^k)^* = (\Pi_h^k)^*(\Pi_h^+, \Phi_h^+, \Pi_h^-, \Phi_h^-), \quad (\Phi_h^k)^* = (\Phi_h^k)^*(\Pi_h^+, \Phi_h^+, \Pi_h^-, \Phi_h^-), \quad (41)$$

where, for example, Π_h^- is an interior boundary value [either $\Pi_h^k(\lambda, a^k)$ or $\Pi_h^k(\lambda, b^k)$] of the approximation defined on D^k , and Π_h^+ is an exterior boundary value [either $\Pi_h^{k-1}(\lambda, b^{k-1})$ or $\Pi_h^{k+1}(\lambda, a^{k+1})$] of the approximation defined on either D^{k-1} or D^{k+1} . The fluxes (41) could also depend on Ψ_h^\pm , but we will not need this extra generality.

Let us now write the $N+1$ equations (40) in matrix form, and also collect the corresponding matrix forms associated with approximation of the Ψ and Π equations. To write down these matrix forms, we first introduce the k th *mass* and *stiffness* matrices,

$$M_{ij}^k = \int_{a^k}^{b^k} d\xi \ell_i^k(\xi) \ell_j^k(\xi), \quad S_{ij}^k = \int_{a^k}^{b^k} d\xi \ell_i^k(\xi) \ell_j^{k'}(\xi). \quad (42)$$

These matrices belong to D^k , and the corresponding matrices belonging to the reference interval $[-1, 1]$ are

$$M_{ij} = \int_{-1}^1 du \ell_i(u) \ell_j(u), \quad S_{ij} = \int_{-1}^1 du \ell_i(u) \ell_j'(u), \quad (43)$$

where $\ell_j(u)$ is the j th Lagrange polynomial determined by the LGL nodes u_j on $[-1, 1]$. These matrices are related by $M_{ij}^k = \frac{1}{2}(b^k - a^k)M_{ij}$ and $S_{ij}^k = S_{ij}$, whence only the reference matrices require computation and storage. In (40) we now expand all polynomial approximations in the Lagrange polynomial basis as in (30), thereby obtaining

$$M^k \partial_\lambda \Phi_h^k + (S^k)^T (\beta^\xi \Phi)_h^k - (S^k)^T \Pi_h^k = [\beta^\xi(\lambda, \xi)(\Phi_h^k)^* - (\Pi_h^k)^*] \ell^k(\xi) \Big|_{a^k}^{b^k}. \quad (44)$$

Now, as described in [15], the spectral collocation derivative matrix is

$$(D^k)_{ij} = \frac{d\ell_j^k}{d\xi} \Big|_{\xi=\xi_i^k}. \quad (45)$$

also given by $D^k = (M^k)^{-1} S^k$. By the symmetry of the mass matrix, $(D^k)^T = (S^k)^T (M^k)^{-1}$. We then introduce the similarity-transformed matrix

$$D_M^k = M^k D^k (M^k)^{-1}, \quad (46)$$

tailored to obey $(D_M^k)^T = (M^k)^{-1} (S^k)^T$. Applying $(M^k)^{-1}$ to both sides of (44) yields an equation for $\partial_\lambda \Phi_h^k$. The result and the corresponding equations for $\partial_\lambda \Psi_h^k$ and $\partial_\lambda \Pi_h^k$ (derived via calculations similar to those presented above) are the following:

$$\partial_\lambda \Psi_h^k - (\beta^\xi \Phi)_h^k + \Pi_h^k = 0 \quad (47a)$$

$$\begin{aligned} \partial_\lambda \Pi_h^k + (D_M^k)^T (\beta^\xi \Pi)_h^k - (D_M^k)^T (x_\xi^{-2} \Phi)_h^k + (x_\xi^{-3} x_{\xi\xi} \Phi)_h^k - (V \Psi)_h^k \\ = (M^k)^{-1} \left[\left(\beta^\xi(\lambda, \xi)(\Pi_h^k)^* - x_\xi^{-2}(\lambda, \xi)(\Phi_h^k)^* \right) \ell^k(\xi) \right] \Big|_{a^k}^{b^k} \end{aligned} \quad (47b)$$

$$\partial_\lambda \Phi_h^k + (D_M^k)^T (\beta^\xi \Phi)_h^k - (D_M^k)^T \Pi_h^k = (M^k)^{-1} \left[\left(\beta^\xi(\lambda, \xi)(\Phi_h^k)^* - (\Pi_h^k)^* \right) \ell^k(\xi) \right] \Big|_{a^k}^{b^k}. \quad (47c)$$

All adjacent vectors in these expressions, e. g. $(\beta^\xi \Phi)_h^k$, $(V \Psi)_h^k$, and $(x_\xi^{-3} x_{\xi\xi} \Phi)_h^k$, should be interpreted as a single vector obtained via component-by-component products.

B. Numerical Flux

To define the vector $(f_\Pi, f_\Phi)^T$ of physical fluxes, we write (27b,c) as

$$\partial_\lambda \begin{pmatrix} \Pi \\ \Phi \end{pmatrix} + \partial_\xi \begin{pmatrix} f_\Pi \\ f_\Phi \end{pmatrix} = \text{lower order terms}. \quad (48)$$

This equation determines the physical and numerical fluxes as follows:

$$\begin{pmatrix} f_\Pi \\ f_\Phi \end{pmatrix} \equiv \begin{pmatrix} -\beta^\xi & x_\xi^{-2} \\ 1 & -\beta^\xi \end{pmatrix} \begin{pmatrix} \Pi \\ \Phi \end{pmatrix}, \quad \begin{pmatrix} (f_\Pi^k)^* \\ (f_\Phi^k)^* \end{pmatrix} \equiv \begin{pmatrix} -\beta^\xi & x_\xi^{-2} \\ 1 & -\beta^\xi \end{pmatrix} \begin{pmatrix} (\Pi_h^k)^* \\ (\Phi_h^k)^* \end{pmatrix}. \quad (49)$$

The combinations of $(\Pi_h^k)^*$ and $(\Phi_h^k)^*$ which appear in (47b,c) are precisely $-(f_\Pi^k)^*$ and $-(f_\Phi^k)^*$, as must be the case since these terms have arisen through integration by parts. In this subsection we construct the required boundary expressions for $(f_\Pi^k)^*$ and $(f_\Phi^k)^*$. Our numerical flux must be robust, ensure stability, and be capable of handling the analytic discontinuities at the particle location. Numerical experiments suggest that inclusion of a Dirac delta function renders inadequate otherwise suitable numerical fluxes, such as the central and Lax–Friedrichs fluxes. However, as we

will see, a suitably modified upwind numerical flux successfully handles the delta functions in the system (27), recovering optimal convergence. We begin by constructing the standard upwind flux corresponding to no particle, and then incorporate the particle's effect into the flux through the addition of an extra term.

An upwind numerical flux passes information across an interface in the direction of propagation. To construct the upwind numerical fluxes, we first diagonalize the matrix appearing in (49) as follows:

$$\begin{pmatrix} -\beta^\xi & x_\xi^{-2} \\ 1 & -\beta^\xi \end{pmatrix} = T \begin{pmatrix} -\beta^\xi + x_\xi^{-1} & 0 \\ 0 & -\beta^\xi - x_\xi^{-1} \end{pmatrix} T^{-1}, \quad T^{-1} = \begin{pmatrix} 1 & x_\xi^{-1} \\ 1 & -x_\xi^{-1} \end{pmatrix}. \quad (50)$$

Application of T^{-1} on the system vector $(\Pi, \Phi)^T$ of fundamental fields yields the system vector $(\Pi + \Phi/x_\xi, \Pi - \Phi/x_\xi)^T$ of characteristic fields. For our problem, the first characteristic field $\Pi + \Phi/x_\xi$ propagates rightward with speed $-\beta^\xi + x_\xi^{-1}$ relative to the $\partial/\partial\lambda$ time axis, while the second characteristic field $\Pi - \Phi/x_\xi$ propagates leftward with speed $-\beta^\xi - x_\xi^{-1}$. Respectively, the upwind fluxes at a left endpoint a^k ($k \neq k_p + 1$) and at a right endpoint b^k ($k \neq k_p$) then take the following forms:

$$\begin{pmatrix} (f_\Pi^k)^* \\ (f_\Phi^k)^* \end{pmatrix}_{\text{left}} = T \begin{pmatrix} 0 & 0 \\ 0 & -\beta^\xi - x_\xi^{-1} \end{pmatrix} T^{-1} \begin{pmatrix} \Pi_h^- \\ \Phi_h^- \end{pmatrix} + T \begin{pmatrix} -\beta^\xi + x_\xi^{-1} & 0 \\ 0 & 0 \end{pmatrix} T^{-1} \begin{pmatrix} \Pi_h^+ \\ \Phi_h^+ \end{pmatrix} \quad (51a)$$

$$\begin{pmatrix} (f_\Pi^k)^* \\ (f_\Phi^k)^* \end{pmatrix}_{\text{right}} = T \begin{pmatrix} 0 & 0 \\ 0 & -\beta^\xi - x_\xi^{-1} \end{pmatrix} T^{-1} \begin{pmatrix} \Pi_h^+ \\ \Phi_h^+ \end{pmatrix} + T \begin{pmatrix} -\beta^\xi + x_\xi^{-1} & 0 \\ 0 & 0 \end{pmatrix} T^{-1} \begin{pmatrix} \Pi_h^- \\ \Phi_h^- \end{pmatrix}. \quad (51b)$$

Eqs. (51a,b) formalize the intuitive concept behind the upwind numerical flux. In these equations triple-product matrices operate on the interior and exterior solution. The first matrix operation transforms the fields to characteristic fields, the second projects out one of the characteristic fields, and the third transforms back to the fundamental fields. As a result, information from a right-moving field, say, influences the subdomain to the right, but not the subdomain to the left.

To achieve succinct expressions for the upwind flux which hold at both left and right endpoints, at each interface we define the average of a numerical variable and its numerical jump as

$$\{\{\Phi\}\} = \frac{1}{2}(\Phi^+ + \Phi^-), \quad [[\Phi]]_{\text{num}} = \mathbf{n}^+ \Phi^+ + \mathbf{n}^- \Phi^-. \quad (52)$$

Here \mathbf{n} denotes the local outward-pointing normal of a subdomain and can be ± 1 . The numerical jump here is not a predetermined analytical jump as defined in Eq. (9), and it has a different sign convention. These definitions yield the following concise formulas (valid at left or right endpoints):

$$(f_\Pi^k)^* = \{\{-\beta^\xi \Pi_h + x_\xi^{-2} \Phi_h\}\} + \frac{1}{2} [[x_\xi^{-1} \Pi_h - x_\xi^{-1} \beta^\xi \Phi_h]]_{\text{num}} \quad (53a)$$

$$(f_\Phi^k)^* = \{\{\Pi_h - \beta^\xi \Phi_h\}\} + \frac{1}{2} [[x_\xi^{-1} \Phi_h - x_\xi \beta^\xi \Pi_h]]_{\text{num}}. \quad (53b)$$

At all interior endpoints (a^k for $k \neq 1, k_p + 1$, and b^k for $k \neq k_p, K$) we will use this numerical flux which is determined by the local numerical solutions. We also use this upwind form at a physical boundary (that is, a^1 or b^K), but in this case a boundary condition supplies the exterior solution.

Turning now to the endpoints $a^{k_p+1} = b^{k_p}$ corresponding to the particle location, we modify the standard upwind flux (53) following the generalized discontinuous Galerkin method outlined in [21]. Consider a Dirac delta function located at the interface between elements D^{k_p} and D^{k_p+1} , and the weak form of the resulting system (27). The relevant new terms to consider have the form

$$\int_{D^{k_p}} d\xi J_{1,2} \delta(\xi - \xi_p) \ell_j^{k_p}(\xi), \quad \int_{D^{k_p+1}} d\xi J_{1,2} \delta(\xi - \xi_p) \ell_j^{k_p+1}(\xi). \quad (54)$$

Upon evaluation, each if these terms appears similar in form to a boundary flux. The discontinuous Galerkin method provides a self-consistent way to evaluate these integrals and then add the results to the numerical flux. We only require the usual selection property of the delta function when integrated over the *union* $D^{k_p} \cup D^{k_p+1}$, and we are free to choose how the individual integrals over D^{k_p} and D^{k_p+1} contribute to the total integral. In fact, the dynamics of (27) suggest a preferred distributional splitting. To see why, consider the scalar advection equation $(\partial_\lambda + v\partial_\xi)u = J(\xi, \lambda)\delta(\xi - \xi_p)$, with $v > 0$. Since this equation corresponds to rightward propagation, the natural choice for the associated distributional splitting of the delta function term is

$$\int_{D^{k_p}} d\xi J\delta(\xi - \xi_p)\ell_j^{k_p}(\xi) = 0, \quad \int_{D^{k_p+1}} d\xi J\delta(\xi - \xi_p)\ell_j^{k_p+1}(\xi) = J(\xi_p, t)\delta_{0,j}. \quad (55)$$

For this case, notice that the delta function only “sees” a single Lagrange polynomial, namely $\ell_0^{k_p+1}(\xi)$ on the rightward interval.

To enact an upwind splitting of the delta functions appearing the system (27), we simply use the matrix T^{-1} already defined in (50) to isolate the two propagating characteristic modes of the system. Consistent with propagation of these modes, at the particle location we modify the fluxes given in Eqs. (51a,b),

$$\begin{pmatrix} (f_\Pi^{k_p+1})^* \\ (f_\Phi^{k_p+1})^* \end{pmatrix}_{\text{left, modified}} = \begin{pmatrix} (f_\Pi^{k_p+1})^* \\ (f_\Phi^{k_p+1})^* \end{pmatrix}_{\text{left}} + T \begin{pmatrix} 1 & 0 \\ 0 & 0 \end{pmatrix} T^{-1} \begin{pmatrix} J_1 \\ J_2 \end{pmatrix} \quad (56a)$$

$$\begin{pmatrix} (f_\Pi^{k_p})^* \\ (f_\Phi^{k_p})^* \end{pmatrix}_{\text{right, modified}} = \begin{pmatrix} (f_\Pi^{k_p})^* \\ (f_\Phi^{k_p})^* \end{pmatrix}_{\text{right}} + T \begin{pmatrix} 0 & 0 \\ 0 & -1 \end{pmatrix} T^{-1} \begin{pmatrix} J_1 \\ J_2 \end{pmatrix}. \quad (56b)$$

The correctness of this prescription can be see as follows. Integration of the system (27) over the union $D^{k_p} \cup D^{k_p+1}$ followed by a subsequent integration by parts on each interval generates the following boundary terms at the particle location (and on the right-hand side of the equal sign):

$$\begin{pmatrix} f_\Pi \\ f_\Phi \end{pmatrix} \Big|_{(\lambda, a^{k_p+1})} - \begin{pmatrix} f_\Pi \\ f_\Phi \end{pmatrix} \Big|_{(\lambda, b^{k_p})} + \begin{pmatrix} J_1 \\ J_2 \end{pmatrix}. \quad (57)$$

The two physical fluxes in this equation of course cancel each other out, leaving only the vector $(J_1, J_2)^T$. Our modifications (56a,b) of the numerical flux are tailored to mimic this result. While the difference of the left/right numerical fluxes at the particle location will not, in general, cancel each other out (due to numerical error), notice that by subtracting (56b) from (56a) we generate precisely the vector $(J_1, J_2)^T$. This argument can be made more rigorous through an analysis based on integrating the two local numerical solutions on D^{k_p} and D^{k_p+1} against the Lagrange polynomials $\ell_N^{k_p}(\xi)$ and $\ell_0^{k_p+1}(\xi)$. Finally, using the general expressions (53a,b), we may likewise succinctly express the modified numerical flux at the particle location as

$$\begin{pmatrix} (f_\Pi^k)^* \\ (f_\Phi^k)^* \end{pmatrix}_{\text{modified}} = \begin{pmatrix} (f_\Pi^k)^* \\ (f_\Phi^k)^* \end{pmatrix} + \frac{1}{2}T \begin{pmatrix} 1 - \mathbf{n}^- & 0 \\ 0 & -1 - \mathbf{n}^- \end{pmatrix} T^{-1} \begin{pmatrix} J_1 \\ J_2 \end{pmatrix}, \quad (58)$$

where either $k = k_p$ or $k = k_p + 1$ in this equation.

C. Initial data and boundary conditions

The issues of initial data and boundary conditions are not part of the dG method *per se*, but we must nevertheless specify both to complete our numerical scheme. We adopt trivial (zero) initial

k	$\text{Re}\beta_{2,k}^{\text{RW}}(500)$	$\text{Im}\beta_{2,k}^{\text{RW}}(500)$	k	$\text{Re}\beta_{2,k}^{\text{Z}}(500)$	$\text{Im}\beta_{2,k}^{\text{Z}}(500)$
1	-1.25849067540E-02	0	1	-1.25789030971E-02	0
2	-8.23918644025E-03	0	2	-8.23529461921E-03	0
3	-5.49064917188E-03	0	3	-5.48806353366E-03	0
4	-3.62410271081E-03	0	4	-3.62239165593E-03	0
5	-2.32805739548E-03	0	5	-2.32695433490E-03	0
6	-1.42584745587E-03	0	6	-1.42517041551E-03	0
7	-8.04688157035E-04	0	7	-8.04304980721E-04	0
8	-3.83719341654E-04	0	8	-3.83535015275E-04	0
9	-2.99532499571E-03	1.73407822255E-03	9	-2.99383340672E-03	1.73321233868E-03

k	$\text{Re}\gamma_{2,k}^{\text{RW}}(500)$	$\text{Im}\gamma_{2,k}^{\text{RW}}(500)$	k	$\text{Re}\gamma_{2,k}^{\text{Z}}(500)$	$\text{Im}\gamma_{2,k}^{\text{Z}}(500)$
1	-8.36957985819E-09	0	1	-8.35513276685E-09	0
2	-2.95922379193E-07	0	2	-2.95425498144E-07	0
3	-2.97720676842E-06	0	3	-2.97239482588E-06	0
4	-8.13540247121E-06	0	4	-8.12342297064E-06	0
5	-1.40566197350E-06	0	5	-1.40379108037E-06	0
6	-5.02202428400E-08	0	6	-5.01539234399E-08	0
7	-1.01094068265E-09	0	7	-1.00959570760E-09	0
8	-7.70486047714E-12	0	8	-7.69439666825E-12	0
9	-2.99056309897E-03	1.73610608573E-03	9	-2.98758843820E-03	1.73437449497E-03

TABLE I: Compressed kernels for $\ell = 2$, $r_b/(2M) = 500$, $\varepsilon = 10^{-10}$. There are $d = 10$ poles and strengths, and complex conjugation of the ninth entries gives the tenth entries. Zeros correspond to outputs from the compression algorithm which are less than 10^{-30} in absolute value.

data, and avoid the issue of an impulsively started problem by smoothly “switching on” the source terms, as discussed in Appendix C. At the boundaries we impose outgoing radiation boundary conditions. Both potentials (2,3) behave differently in the $\xi \rightarrow -\infty$ and $\xi \rightarrow \infty$ limits, whence we treat the cases $\xi = a$ and $\xi = b$ differently. Since $1 - 2Mr^{-1} = 2Mr^{-1} \exp(-r/(2M)) \exp(x/(2M))$, in the $x \rightarrow -\infty$, $r \rightarrow 2M^+$ limit both potentials are exponentially small. Therefore, with a being sufficiently negative, $|V^{\text{RW,Z}}(r)|$ is zero to machine precision when r corresponds to $\xi \simeq a$, and as an excellent approximation we may use the Sommerfeld boundary condition

$$(\partial_t \Psi - \partial_x \Psi)(\lambda, a) = 0 \rightarrow \Pi(\lambda, a) + \Phi(\lambda, a)/x_\xi(\lambda, a) = 0. \quad (59)$$

In the $x, r \rightarrow \infty$ limit, both the Zerilli and Regge–Wheeler potentials (2,3) behave like $V^{\text{RW,Z}} = \ell(\ell+1)r^{-2} + O(r^{-3})$. Therefore, were we to adopt a naive Sommerfeld condition at $\xi = b$, the slow fall-off of the potential would corrupt the benefits of our high-order accurate method. Instead, we implement the radiation boundary condition described in [22],

$$-\Pi(\lambda, b) + \Phi(\lambda, b)/x_\xi(\lambda, b) = \frac{f(r_b)}{r_b} \int_0^\lambda \Omega_\ell^{\text{RW,Z}}(\lambda - \lambda', r_b) \Psi(\lambda', b) d\lambda', \quad (60)$$

where $r_b = r(x(\lambda, b)) = r(b)$ and $\Omega_\ell^{\text{RW,Z}}$ is a time-domain boundary kernel. As indicated, this kernel is different for the Regge–Wheeler (here spin-2) and Zerilli cases, although we suppress this dependence wherever possible.

We approximate the time-domain boundary kernel $\Omega_\ell \simeq \Xi_\ell$ as a sum of exponentials

$$\Xi_\ell(t, r_b) = \sum_{k=1}^d \Xi_{\ell,k}(t, r_b), \quad \Xi_{\ell,k}(t, r_b) = \frac{\gamma_{\ell,k}(r_b/(2M))}{2M} \exp\left(\frac{t\beta_{\ell,k}(r_b/(2M))}{2M}\right). \quad (61)$$

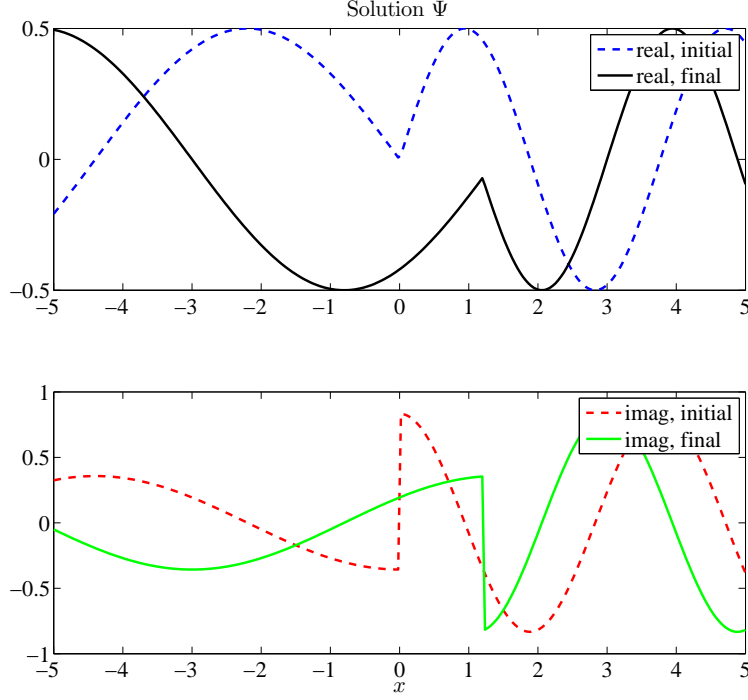


FIG. 1: Ψ -COMPONENT OF THE SOLUTION. The Π and Φ components are qualitatively similar.

The parameters $\gamma_{\ell,k}(r_b/(2M))$ and $\beta_{\ell,k}(r_b/(2M))$ determine the approximation $\Xi_\ell(t, r_b)$, and they depend on the Regge–Wheeler or Zerilli case, the orbital index ℓ , and the dimensionless boundary radius $r_b/(2M)$. The approximation Ξ_ℓ is designed so that its Laplace transform agrees with the transform of Ω_ℓ to relative supremum error ε along the axis of imaginary Laplace frequency, and the parameters $\gamma_{\ell,k}$ and $\beta_{\ell,k}$ are the outputs from the Alpert–Greengard–Hagstrom compression algorithm [22, 23]. Theoretically, ε is a long-time bound on the relative convolution error in the time domain, and it measures the accuracy of the boundary condition. Table I collects the $\ell = 2$ kernels for $r_b = 1000M$ and $\varepsilon = 10^{-10}$. We evolve the constituent pieces of the approximate convolution via temporal integration of the ODE

$$\frac{d}{d\lambda} \int_0^\lambda \Xi_{\ell,k}(\lambda - \lambda', r_b) \Psi(\lambda', b) d\lambda' = \frac{\beta_{\ell,k}}{2M} \int_0^\lambda \Xi_{\ell,k}(\lambda - \lambda', r_b) \Psi(\lambda', b) d\lambda' + \Xi_{\ell,k}(0, r_b) \Psi(\lambda, b), \quad (62)$$

carrying out the integration along side, and coupled with, the numerical evolution of the system (27). With this boundary condition, we are free to choose essentially any boundary $\xi = b$, so long as it lies to the right of the source. Our outer radiation boundary condition is especially useful when studying eccentric orbits, for which one must average quantities over many periods.

IV. NUMERICAL EXPERIMENTS AND RESULTS

A. Forced ordinary 1+1 wave equation

We consider two scenarios involving an exact solution of the distributionally forced 1+1 wave equation with no potential. The first adopts exact initial data, and the second trivial data in parallel with the blackhole perturbation problem (a setting where trivial data is often chosen).

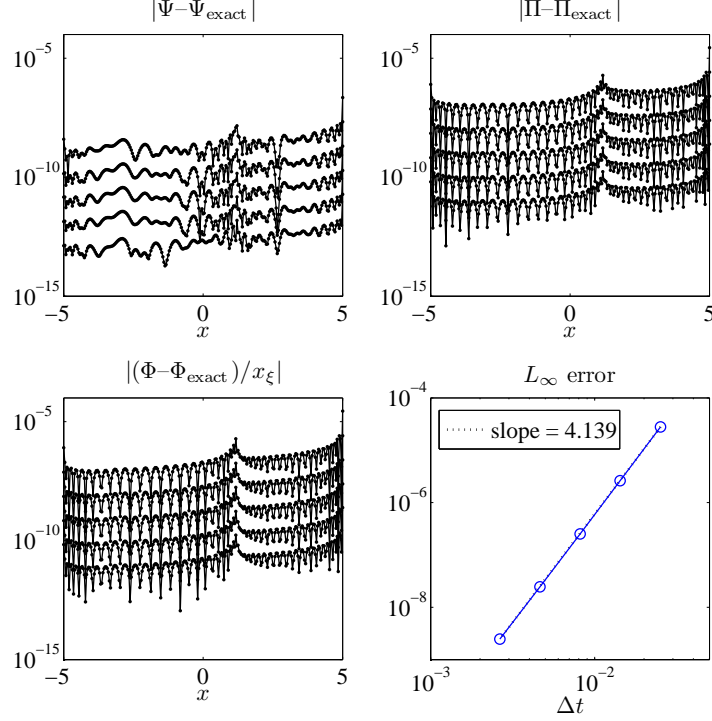


FIG. 2: TEMPORAL CONVERGENCE OF THE LINEARLY MOVING PARTICLE EXPERIMENT. Errors have been computed relative to a uniformly spaced x -grid and over all fields. The dotted line is a least-squares fit of the data points (the round circles).

1. Wave equation with exact initial data

For a fixed velocity v obeying $|v| < 1$, we consider

$$-\partial_t^2 \Psi + \partial_x^2 \Psi = \cos t\delta(x - vt) + i \cos t\delta'(x - vt). \quad (63)$$

Closed-form exact solutions for the real and imaginary parts of Ψ are given in Appendix B, and we will check the convergence of our numerically generated solution against the complexification of these exact solutions. After expressing (63) as a first order system and adopting our dG scheme, we obtain the same equations as in (47), except now with a zero potential vector \mathbf{V} . Our domain is comprised of two subdomains: D^1 to the left of the particle location $x_p(t) = vt$, and D^2 to the right of $x_p(t)$. At $x_p(t)$, the interface between D^1 and D^2 , we use Eq. (58) for the numerical fluxes $(f_{\Pi}^k)^*$ and $(f_{\Phi}^k)^*$. At the physical boundary points we choose fluxes which enforce simple Sommerfeld boundary conditions,

$$\Pi(\lambda, a) + \Phi(\lambda, a)/x_{\xi}(\lambda, a) = 0, \quad \Pi(\lambda, b) - \Phi(\lambda, b)/x_{\xi}(\lambda, b) = 0. \quad (64)$$

For this first experiment, we take initial data from the exact solution.

Working with the global domain $[a, b] = [-5, 5]$, we choose $v = 0.4$ and the final time $t_F = 3.0$. For these choices the critical ξ value (17) always lies outside of the global domain, although clearly the example becomes pathological for a final time t_F near 12.5 (when the particle crosses the outer boundary). Fig. 1 shows the Ψ component of the solution vector, and the Φ and Π components also feature moving discontinuities. Fig. 2 documents the accuracy after several evolutions, each

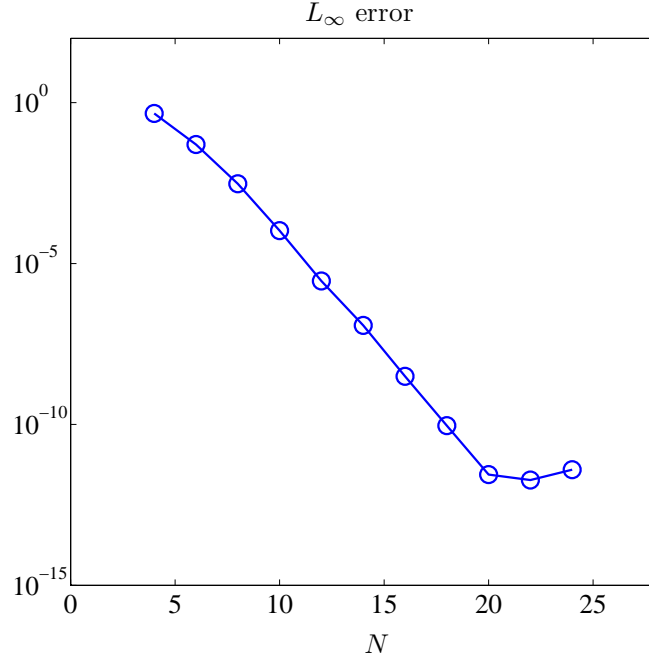


FIG. 3: SPECTRAL CONVERGENCE OF THE LINEARLY MOVING PARTICLE EXPERIMENT. Again, errors have been computed relative to a uniformly spaced x -grid and over all fields.

with $N = 26$ points, performed with decreasing temporal resolution in order to exhibit the fourth-order accuracy of the temporal Runge–Kutta integration. To compute errors, we have used the polynomial representations of the two local solutions, each computed with respect to the coordinates (λ, ξ) , to interpolate onto a uniformly spaced x -grid with 256 points where L_∞ errors have been calculated. Fig. 3 demonstrates the spectral convergence of our method for this problem. Here N is the number of points on each of the two subdomains, and for each N we have chosen a Δt to ensure stability.

2. Wave equation with trivial initial data

In this scenario we again consider (63), although now choosing $v = 0$ (a fixed particle analogous to a circular orbit) and trivial initial data $\Psi = \Pi = \Phi = 0$. As before, we will compute errors over all fields, after interpolation onto a reference grid, and against the exact solution. Before computing errors for the Ψ variable when adopting trivial initial data, we have found it necessary to adjust the mean of our numerically generated Ψ in order to ensure that it equals the mean of the exact Ψ . For the problem (63) with Sommerfeld boundary conditions (64), the Ψ component of the solution vector is only determined up to an additive constant. Due to the presence of the potential, no such ambiguity is associated with solving (1).

Our first test involves the minimal two domain set up. Since the problem is now impulsively started, we smooth the source functions as described in Eq. (C1), choosing $t_0 = 0$, $\tau = 3$, and $\delta = 10$. For these choices, the source is smoothly “switched on” (to machine precision) and is fully on by $t = 3$. Resolution of the transition requires relatively many points, and we have chosen $N = 61$ on each subdomain. For the final time $t_F = 10$, we demonstrate temporal convergence in the left panel of Fig. 4. We note that, as indicated in the figure, convergence is abruptly lost without the smoother. However, even without the smoother, by adopting multiple subdomains

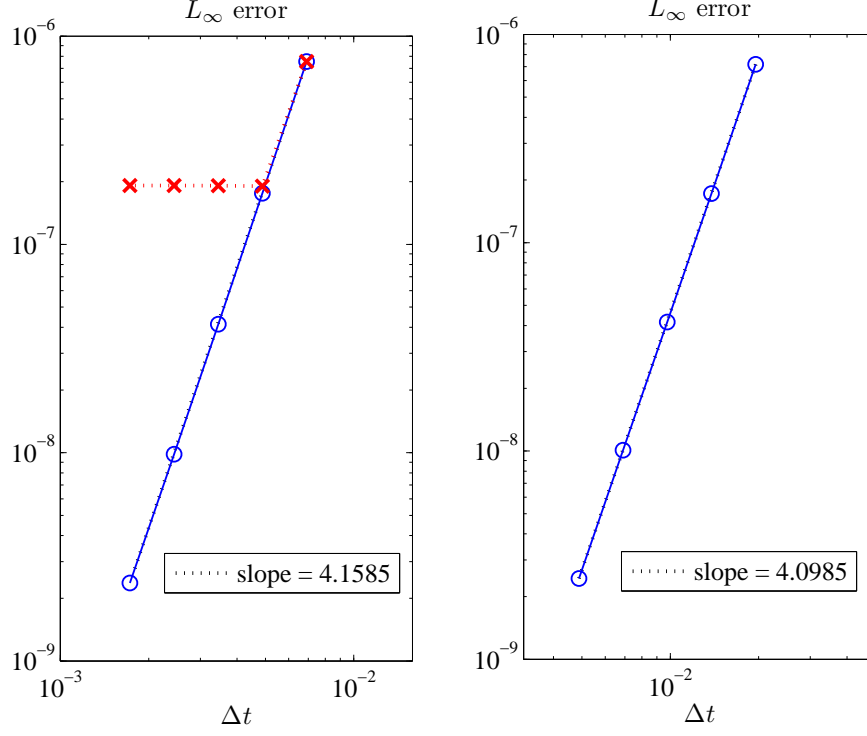


FIG. 4: TEMPORAL CONVERGENCE WITH TRIVIAL INITIAL DATA. The left panel compares the two-domain experiment run with and without the smoother, denoted by circles and crosses respectively. The right panel corresponds to multiple subdomains and no smoother. As described in the text, on each subdomain we have fixed the mean of the numerical Ψ to the exact value before computing errors.

we also recover convergence to the exact solution (of course assuming $t_F > 5$, so that the initial incorrect profiles can fully propagate off the domain). Indeed, the right panel of Fig. 4 documents the results for the same problem, but now without smoothing and 20 subdomains, each with $N = 7$ points. We explain this observation by noting that for $N = 1$ our dG method formally becomes a FV method. Therefore, many low-order elements corresponds to a more dissipative numerical flux, and the extra dissipation smooths the oscillations stemming from our impulsively started problem.

B. Blackhole perturbations

1. Experiment: Zerilli equation with radiation boundary conditions

This experiment involves the $\ell = 2$, $m = 2$ polar problem and a circular orbit with $p = 7.9456$, $M = 1$, and $m_p = 1$. We choose trivial initial data at $t_0 = 0$, with a smoother defined by $\tau = 10$ and $\delta = 10$. Integrating to final time $t_F = 90$, we first generate an accurate reference solution Ψ_{ref} on the domain $[-100, 100]$, using 65+55 subdomains (65 to the left of the particle and 55 to the right) with $N = 37$ nodal points on each. Here and below, we choose the time step Δt to ensure stability. At both endpoints $x = \pm 100$ we place Sommerfeld boundary conditions on Ψ_{ref} , as physically no radiation reaches the endpoints by the final time.

The experiment is to generate a second numerical solution Ψ on the shorter domain $[-50, b]$, where $b = 30 + 2 \log(15 - 1) \simeq 35.2$. We again evolve to final time $t_F = 90$, now with the convolution radiation boundary condition (60) placed at the outer endpoint $x = b$. The relevant Zerilli kernel

is defined in Table II of Ref. [22]. This kernel corresponds to $r_b/(2M) = 15$ and the tolerance $\varepsilon = 10^{-10}$. At the inner endpoint $x = -50$ we again adopt a Sommerfeld boundary condition. For 30+15 subdomains with 33 points on each, the corresponding Ψ is then compared against the reference solution Ψ_{ref} in the L_∞ norm. After interpolation onto a uniformly spaced grid with 853 points, we have found that $\|\Psi - \Psi_{\text{ref}}\|_\infty \simeq 8.2314 \times 10^{-12}$.

2. Results: circular orbits

This subsection compares our numerical results for circular orbits to those obtained by other authors. For brevity we restrict ourselves to $\ell = 2$, but note that our method maintains its performance for higher ℓ . We have considered higher ℓ values, and a fuller compilation of our results will appear elsewhere. For our simulations, we have chosen³ $M = 1 = m_p$, with $\xi_{\text{max}} = x_{\text{max}} = 1000 + 2 \log(500 - 1) \simeq 1012$ and $\xi_{\text{min}} = x_{\text{min}} = -200$ as the outer and inner boundaries. We have used 45+200 subdomains, each with $N = 21$ points, and a smoother (C1) defined by $\tau = 1000$ and $\delta = 0.0002$. For these choices, we have integrated to $t_F = 2500$ with time step $\Delta t = 0.005$. With these parameters we compute waveforms with a relative error of better than 10^{-8} . Radiation boundary conditions (60) have been enforced through Table I. Other parameters or non-uniformly placed subdomains may prove advantageous, but we have not explored all possibilities.

We first describe what we have measured. The luminosities of gravitational energy and angular momentum across an arbitrarily large spherical surface are determined from the master functions $\Psi_{\ell m}^{\text{CPM}}(u + x, r)$ and $\Psi_{\ell m}^{\text{Z}}(u + x, r)$. We view the retarded time $u = t - x$ as fixed, but with r, x arbitrarily large. Note that $x \sim r$, as $r \rightarrow \infty$. In the $r \rightarrow \infty$ limit we have the energy and angular momentum luminosities across an infinite-radius spherical surface given by (see [8, 9] and references therein)

$$\dot{E} = \sum_{\ell \geq 2} \sum_{m=-\ell}^{\ell} \dot{E}_{\ell m}, \quad \dot{E}_{\ell m} = \frac{1}{64\pi} \frac{(\ell+2)!}{(\ell-2)!} (|\dot{\Psi}_{\ell m}^{\text{CPM}}|^2 + |\dot{\Psi}_{\ell m}^{\text{ZM}}|^2) \quad (65a)$$

$$\dot{L} = \sum_{\ell \geq 2} \sum_{m=-\ell}^{\ell} \dot{L}_{\ell m}, \quad \dot{L}_{\ell m} = \frac{im}{64\pi} \frac{(\ell+2)!}{(\ell-2)!} (\bar{\Psi}_{\ell m}^{\text{CPM}} \dot{\Psi}_{\ell m}^{\text{CPM}} + \bar{\Psi}_{\ell m}^{\text{ZM}} \dot{\Psi}_{\ell m}^{\text{ZM}}). \quad (65b)$$

Here the overbar and dot denote complex conjugation and time differentiation respectively. The individual multipole contributions ($\dot{E}_{\ell m}$ and $\dot{L}_{\ell m}$) to the total energy and angular momentum luminosities decay exponentially with ℓ [18, 24, 25]. A few simplifications concerning $\dot{E}_{\ell m}$ and $\dot{L}_{\ell m}$ are worth noting. First, due to the fact that the particle moves in the equatorial plane, the following conditions hold: $\ell + m$ even $\implies \Psi^{\text{CPM}} = 0$ and $\ell + m$ odd $\implies \Psi^{\text{ZM}} = 0$. To establish these conditions, note, for example, that when $\ell + m$ is even the axial source terms $F_{\ell m}^{\text{CPM}}$ and $G_{\ell m}^{\text{CPM}}$ are identically zero. Second, from the behavior of the master functions under the mapping $m \rightarrow -m$, we have $\dot{E}_{\ell, m} = \dot{E}_{\ell, -m}$ and $\dot{L}_{\ell, m} = \dot{L}_{\ell, -m}$ [18].

We stress that Eqs. (65a,b) hold at infinity, and practically one must devise a way to extract the waveforms at infinity from the finite computation domain. This problem has been solved for waves on flat spacetime by Abrahams and Evans [26, 27]. We will either simply “read off” waveforms at $r_{\text{max}} = 1000$ or use Abrahams–Evans *flatspace* extraction. For $\ell = 2$ the procedure is as follows. We record a master scalar Ψ at the outer boundary $x = b$ as a time series, and then integrate

³ By dividing Eq. (1) by m_p we can solve for the per-particle-mass perturbation Ψ/m_p (from the coding standpoint, this is equivalent to setting $m_p = 1$). Physical waveforms and other quantities can then be recovered via multiplication by appropriate powers of m_p .

Energy luminosity $(\dot{E}_{2m} + \dot{E}_{2,-m})/m_p^2$					
m	dG, read off	dG, extract	FE	FR	FD
1	$8.17530620 \times 10^{-7}$	8.1633×10^{-7}	8.1662×10^{-7}	8.1633×10^{-7}	8.1623×10^{-7}
2	$1.70685914 \times 10^{-4}$	1.7062×10^{-4}	1.7064×10^{-4}	1.7063×10^{-4}	1.7051×10^{-4}

Angular momentum luminosity $(\dot{L}_{2m} + \dot{L}_{2,-m})/m_p^2$					
m	dG, read off	dG, extract	FE	FR	FD
1	$1.83102416 \times 10^{-5}$	1.8283×10^{-5}	1.8289×10^{-5}	1.8283×10^{-5}	1.8270×10^{-5}
2	$3.82285415 \times 10^{-3}$	3.8215×10^{-3}	3.8219×10^{-3}	3.8215×10^{-3}	3.8164×10^{-3}

TABLE II: $\ell = 2$ LUMINOSITIES FOR A CIRCULAR ORBIT WITH $(p, e) = (7.9456, 0)$.

Total $\ell = 2$ energy luminosity $m_p^{-2} \sum_{m=-2}^2 \langle \dot{E}_{2m} \rangle$			
Orbit parameters	dG, read off	dG, extract	FR
$e = 0.18891539, p = 7.50477840$	2.59367×10^{-4}	2.59296×10^{-4}	2.59296×10^{-4}
$e = 0.76412402, p = 8.75456059$	1.57146×10^{-4}	1.57120×10^{-4}	1.57131×10^{-4}

Total $\ell = 2$ angular momentum luminosity $m_p^{-2} \sum_{m=-2}^2 \langle \dot{L}_{2m} \rangle$			
Orbit parameters	dG, read off	dG, extract	FR
$e = 0.18891539, p = 7.50477840$	4.91165×10^{-3}	4.91018×10^{-3}	4.91016×10^{-3}
$e = 0.76412402, p = 8.75456059$	2.09297×10^{-3}	2.09220×10^{-3}	2.09221×10^{-3}

TABLE III: TOTAL $\ell = 2$ LUMINOSITIES FOR ECCENTRIC ORBITS.

$\Psi(t, b) \simeq \ddot{f}(t - b) + 3\dot{f}(t - b)b^{-1} + 3f(t - b)b^{-2}$ as if it were exact, thereby recovering the profile $f(t)$ and its derivatives. We perform a similar extraction on Π . The Abrahams–Evans procedure is not exact for the perturbation equations we consider. Nevertheless, upon substitution of the approximate expansion $\ddot{f}(t - x) + 3\dot{f}(t - x)x^{-1} + 3f(t - x)x^{-2}$ into one of the (homogeneous) master equations (1), we find a residual which is $O(r^{-3} \log(\frac{1}{2}r/M))$. Table II compares our dG, circular-orbit, and $\ell = 2$ energy and angular momentum luminosities to results obtained by other numerical methods described in the literature. Such a comparison is not straightforward as the finite-element (FE) results of Sopuerta and Laguna [9] involved reading off the master functions at $x = 2000$, while the finite-difference (FD) results of Martel [18] involved read-off at $x = 1500$ (here we always assume $M = 1$). The frequency-domain (FR) results of Poisson, as reported in [18], for the wave forms at infinity rely on the appropriate boundary value problems in the frequency domain, and of the three should afford the most direct comparisons.

3. Results: eccentric orbits

This subsection compares our numerical results for eccentric orbits to the frequency (FR) domain results of Tanaka *et al* [28] (rather than Poisson’s frequency domain results). We again choose 45+200 subdomains, each with $N = 21$ points, and $\Delta t \simeq 0.01$. Due to the incommensurate radial T_r and azimuthal T_ϕ periods, we encounter the standard difficulty in obtaining measurements from eccentric-orbit simulations. Ideally, we would average measured luminosities over an infinite time, but will content ourselves with averaging over 4 radial cycles. Given a time series $A(t)$, we compute its corresponding average as

$$\langle A \rangle \equiv \frac{1}{T_2 - T_1} \int_{T_1}^{T_2} dt A(t), \quad T_2 - T_1 = 4T_r. \quad (66)$$

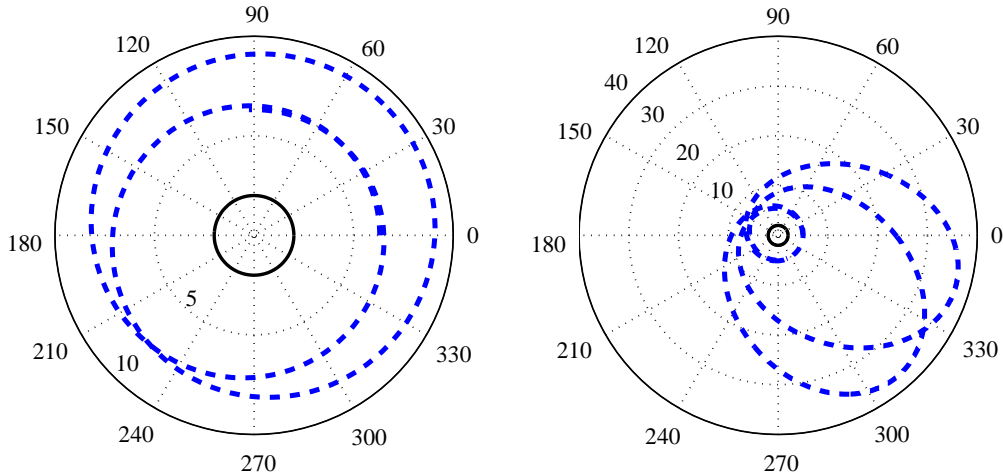


FIG. 5: ORBITAL PATHS. The left panel shows one orbital period for $(e, p) = (0.18891539, 7.50477840)$. The right panel shows two orbital periods for $(e, p) = (0.76412402, 8.75456059)$. In each case the dark inner circle is the horizon. We have used the (r, ϕ) system to construct these polar plots.

Table III compares our total $\ell = 2$ angular momentum and energy luminosities to the frequency (FR) domain results of Ref. [28]. In that reference the authors claim a relative numerical error of better than 10^{-4} , which we have confirmed. We have retained enough significant digits in (e, p) to match the parameters (E_p, L_p) chosen in that reference. While we achieve relative errors of better than 10^{-4} for our *averaged* and *extracted* luminosities, we achieve single precision accuracy for our waveforms as a time series at $x = b$. Figure 5 exhibits the orbital paths for the two cases considered in this subsection, and Fig. 6 shows the corresponding waveforms.

V. CONCLUSION

We have presented a high-order accurate discontinuous Galerkin method for computing gravitational waveforms from extreme mass ratio binaries. Time-domain approaches for computing such waveforms have been hampered by the presence of distributional source terms (which include both a moving Dirac delta function and its derivative) in the governing master equations. By writing a master equation as a first order system, we have treated the source term physically through an appropriate modification to the numerical flux function. Our method maintains spectral convergence without requiring additional procedures (e.g. filtering), even pointwise in the immediate vicinity of the moving discontinuity. Through the use of convolution radiation boundary conditions, we have read-off waveforms at outer boundaries, thereby reducing computational cost without spoiling the high-order accuracy of our method. Accurate (read-off) waveforms, often with a relative error of better than 10^{-8} , have been routinely observed in the course of our simulations.

This work has assumed that the particle trajectory is a timelike geodesic of the Schwarzschild geometry. However, the gravitational perturbations induced by the particle will, in turn, affect the particle trajectory. Several existing techniques capture this effect, thereby incorporating more realistic inspiral (and possibly plunge) into the model. These include gravitational self-force constructions [13, 29, 30, 31] (a representative, but far from exhaustive list), as well as post-Newtonian calculations [32] and adiabatic approximations [4].

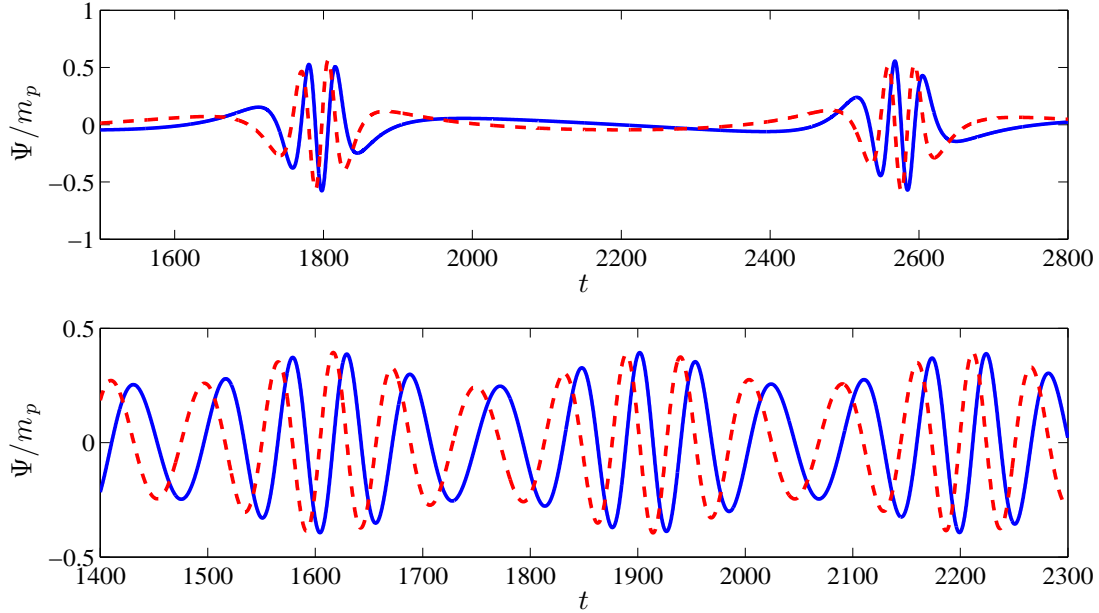


FIG. 6: WAVEFORMS FOR $\ell = 2$, $m = 2$. The top panel shows the $(e, p) = (0.76412402, 8.75456059)$ extracted waveform, and the bottom panel the $(e, p) = (0.18891539, 7.50477840)$ extracted waveform. Solid blue lines and dashed red lines respectively correspond to real and imaginary parts.

We believe that the central ideas of our approach might apply to many of these more sophisticated models. Computation of gravitational self-force requires that metric perturbations are regularized at the location of the particle. Mode-sum regularization has been carried out in the Lorenz gauge [30], in an approach where the metric perturbations are described by the full coupled system of 10 PDEs rather than the simpler master equation description. Although a dG approach might certainly be applied in this setting, our methods are directly applicable to approaches based on master equations. Retaining the master equation description, Detweiler has argued for regularizing gauge-invariant quantities [31]. He has identified the appropriate quantities for quasi-circular orbits, and results based on these variables agree with corresponding Lorenz-gauge computations [33]. Our numerical method should prove ideal for self-force computations which require that the metric perturbations are well resolved near the particle. In particular, we hope to use our method in tandem with self-force corrections based on regularization of gauge-invariant quantities, at least for quasi-circular orbits. The post-Newtonian approach of Ref. [32] is also based on master equations, and we might also follow that reference in order to include nonconservative effects in our simulations.

In adapting our dG method to include, say, self-force effects we would surely encounter new difficulties. For example, due to dissipation associated with a self-force, the particle will inspiral, plunge, and merge with the blackhole. To handle all dynamical phases with our method, we would likely need to regrid at some point during the evolution. However, we believe this issue could be dealt with straightforwardly, given the robustness of the general method.

We conclude with remarks on the applicability of our dG method to perturbations of the Kerr metric. Here, we consider only the scenario of a particle following a timelike geodesic of the Kerr geometry, although one might further consider gravitational self-force for this scenario as well. Now the relevant wave equation, the forced Teukolsky equation, is inherently 2+1 dimensional in the time-domain. In this case we would need to ensure that the particle always lies on an edge

between adjacent subdomains (in this case triangles). Clearly, this is a geometrically different problem, but Fan *et al* [21] have also considered 2+1 problems, and one might pursue the Kerr problem along similar lines.

Acknowledgments

We would like to thank Jae-Hun Jung, Carlos Sopena, and Richard Price for correspondence and useful discussions, and gratefully acknowledge support through grants DMS 0554377 and DARPA/AFOSR FA9550-05-1-0108 to Brown University.

APPENDIX A: JUMP CONDITIONS

The derivation of the jump conditions (7) goes as follows. Using the selection properties of $\delta'(u)$ as a distribution, we first rewrite (1) as

$$\begin{aligned} -\partial_t^2 \Psi + \partial_x^2 \Psi - V(r)\Psi &= f_p(t)F(t, r_p(t))\delta'(r - r_p(t)) \\ &+ [f_p(t)G(t, r_p(t)) - g_p(t)F(t, r_p(t)) - f_p(t)F_r(t, r_p(t))]\delta(r - r_p(t)), \end{aligned} \quad (\text{A1})$$

using the shorthand notations from (8). Next, with L for “left” and R for “right”, we let

$$\Psi(t, r) = \Psi^L(t, r)\theta(r_p(t) - r) + \Psi^R(t, r)\theta(r - r_p(t)), \quad (\text{A2})$$

where the step function $\theta(u)$ obeys $\theta(u) = 0$ for $u < 0$, and $\theta(u) = 1$ for $u > 0$. We view the functions $\Psi^{L,R}$ as everywhere satisfying the homogeneous PDE

$$-\partial_t^2 \Psi^{L,R} + \partial_x^2 \Psi^{L,R} - V(r)\Psi^{L,R} = 0, \quad (\text{A3})$$

even across the particle location $r_p(t)$.

To complete our derivation of (7), we calculate the distributional derivatives of Ψ as given in (A2), insert them into (A1), and then compare terms. Using $\partial/\partial x = f\partial/\partial r$, the identity $\theta'(u) = \delta(u)$, and the argument symmetry of $\delta(u)$, we first compute

$$\partial_x \Psi = \Psi_x^L \theta(r_p(t) - r) + \Psi_x^R \theta(r - r_p(t)) - f\Psi^L \delta(r - r_p(t)) + f\Psi^R \delta(r - r_p(t)), \quad (\text{A4})$$

where on the right-hand side we have switched to subscript notation for partial derivatives. The second x -derivative of (A2) is then

$$\begin{aligned} \partial_x^2 \Psi &= \Psi_{xx}^L \theta(r_p(t) - r) + \Psi_{xx}^R \theta(r - r_p(t)) - 2f^2 \Psi_r^L \delta(r - r_p(t)) + 2f^2 \Psi_r^R \delta(r - r_p(t)) \\ &- f f' \Psi^L \delta(r - r_p(t)) + f f' \Psi^R \delta(r - r_p(t)) - f^2 \Psi^L \delta'(r - r_p(t)) + f^2 \Psi^R \delta'(r - r_p(t)). \end{aligned} \quad (\text{A5})$$

Expressed compactly, the last formula is

$$\begin{aligned} \partial_x^2 \Psi &= \Psi_{xx}^L \theta(r_p(t) - r) + \Psi_{xx}^R \theta(r - r_p(t)) + f_p^2(t) [[\Psi_r]] \delta(r - r_p(t)) \\ &- f_p(t) g_p(t) [[\Psi]] \delta(r - r_p(t)) + f_p^2(t) [[\Psi]] \delta'(r - r_p(t)), \end{aligned} \quad (\text{A6})$$

where the definition (9) is here $[[\Psi]](t) \equiv \Psi^R(t, r_p(t)) - \Psi^L(t, r_p(t))$. To reach Eq. (A6) from the previous line, we have used the selection properties of $\delta'(u)$. Next, we similarly compute

$$\begin{aligned} \partial_t^2 \Psi &= \Psi_{tt}^L \theta(r_p(t) - r) + \Psi_{tt}^R \theta(r - r_p(t)) + 2\dot{r}_p \Psi_t^L \delta(r - r_p(t)) - 2\dot{r}_p \Psi_t^R \delta(r - r_p(t)) \\ &+ \ddot{r}_p \Psi^L \delta(r - r_p(t)) - \ddot{r}_p \Psi^R \delta(r - r_p(t)) - \dot{r}_p^2 \Psi^L \delta'(r - r_p(t)) + \dot{r}_p^2 \Psi^R \delta'(r - r_p(t)). \end{aligned} \quad (\text{A7})$$

The last formula may be written in the succinct form

$$\begin{aligned} \partial_t^2 \Psi &= \Psi_{tt}^L \theta(r_p(t) - r) + \Psi_{tt}^R \theta(r - r_p(t)) - 2\dot{r}_p(t) [[\Psi_t]] \delta(r - r_p(t)) \\ &\quad - \ddot{r}_p(t) [[\Psi]] \delta(r - r_p(t)) - \dot{r}_p^2(t) [[\Psi_r]] \delta(r - r_p(t)) + \dot{r}_p^2(t) [[\Psi]] \delta'(r - r_p(t)), \end{aligned} \quad (\text{A8})$$

again by using the properties of $\delta'(u)$. Finally, with $\partial_t [[\Psi]] = [[\Psi_t]] + \dot{r}_p(t) [[\Psi_r]]$, we rewrite the last expression as

$$\begin{aligned} \partial_t^2 \Psi &= \Psi_{tt}^L \theta(r_p(t) - r) + \Psi_{tt}^R \theta(r - r_p(t)) - 2\dot{r}_p(t) (\partial_t [[\Psi]]) \delta(r - r_p(t)) \\ &\quad - \ddot{r}_p(t) [[\Psi]] \delta(r - r_p(t)) + \dot{r}_p^2(t) [[\Psi_r]] \delta(r - r_p(t)) + \dot{r}_p^2(t) [[\Psi]] \delta'(r - r_p(t)). \end{aligned} \quad (\text{A9})$$

Substitution of (A6) and (A9) into (A1), along with the fact that Ψ^R and Ψ^L solve the homogeneous PDE (A3), then yields Eqs. (7a) and (7b).

APPENDIX B: EXACT SOLUTIONS TO THE FORCED 1+1 WAVE EQUATION

This appendix presents exact solutions to the distributionally forced 1+1 wave equation. Precisely, we consider the equation

$$-\partial_t^2 \Psi + \partial_x^2 \Psi = G(t) \delta(x - vt) + F(t) \delta'(x - vt), \quad (\text{B1})$$

where either $F(t) = 0, G(t) = \cos t$ or $F(t) = \cos t, G(t) = 0$. In analyzing both cases, we make use of the following distributional identities:

$$\partial_u |u| = \text{sgn } u, \quad \partial_u \text{sgn } u = 2\delta(u), \quad (\text{sgn } u)^2 = 1, \quad (\text{B2})$$

with $\text{sgn } u \equiv u/|u|$ the sign function. Throughout, the particle location $x_p(t) = vt$ has linear time dependence, with corresponding speed $|v| < 1$.

1. Solution for $F(t) = 0, G(t) = \cos t$

Following analysis similar to that presented in Section II B [or by substituting the correspondences $x_p(t) = r_p(t)$, $x = r$, $f(r) = 1$, $f'(r) = 0$, and $\ddot{r}(t) = 0$ into the general jumps (7)], we find the jump relations

$$[[\Psi]]_{x=vt} = 0, \quad [[\partial_x \Psi]]_{x=vt} = \gamma^2 \cos t, \quad [[\partial_t \Psi]]_{x=vt} = -v\gamma^2 \cos t, \quad (\text{B3})$$

where $\gamma = (1 - v^2)^{-1/2}$ is the usual relativistic factor. The particular solution

$$\Psi(t, x) = -\frac{1}{2} \sin \vartheta, \quad \vartheta = \gamma^2 (t - xv - |x - vt|) \quad (\text{B4})$$

to Eq. (B1) possess the jumps listed in (B3). Using the identities (B2), let us verify that (B4) indeed solves (B1) for $F(t) = 0$ and $G(t) = \cos t$. Straightforward computation of the first and second order t -derivatives yields

$$\partial_t \Psi = -\frac{1}{2} \gamma^2 [1 + v \text{sgn}(x - vt)] \cos \vartheta \quad (\text{B5})$$

$$\partial_t^2 \Psi = \frac{1}{2} \gamma^4 [1 + v \text{sgn}(x - vt)]^2 \sin \vartheta + v^2 \gamma^2 \delta(x - vt) \cos \vartheta. \quad (\text{B6})$$

while for the x -derivatives we similarly find

$$\partial_x \Psi = \frac{1}{2} \gamma^2 [v + \text{sgn}(x - vt)] \cos \vartheta \quad (\text{B7})$$

$$\partial_x^2 \Psi = \frac{1}{2} \gamma^4 [v + \text{sgn}(x - vt)]^2 \sin \vartheta + \gamma^2 \delta(x - vt) \cos \vartheta. \quad (\text{B8})$$

Forming $-\partial_t^2 \Psi + \partial_x^2 \Psi = \delta(x - vt) \cos \vartheta$, we then appeal to the selection property of the delta function in order to reach the desired result, $-\partial_t^2 \Psi + \partial_x^2 \Psi = \delta(x - vt) \cos t$.

2. Solution for $F(t) = \cos t$, $G(t) = 0$

The jump relations for this case are

$$[[\Psi]]_{x=vt} = \gamma^2 \cos t, \quad [[\partial_x \Psi]]_{x=vt} = 2v\gamma^4 \sin t, \quad [[\partial_t \Psi]]_{x=vt} = -(1+v^2)\gamma^4 \sin t. \quad (\text{B9})$$

Now a particular solution to (B1) is

$$\Psi(t, x) = \frac{1}{2}\gamma^2[v + \text{sgn}(x - vt)] \cos \vartheta, \quad \vartheta = \gamma^2(t - xv - |x - vt|). \quad (\text{B10})$$

To verify that (B10) indeed solves (B1) for $F(t) = \cos t$ and $G(t) = 0$, we first calculate

$$\partial_t \Psi = -\frac{1}{2}\gamma^4[2v + (1+v^2)\text{sgn}(x - vt)] \sin \vartheta - v\gamma^2 \delta(x - vt) \cos \vartheta \quad (\text{B11})$$

$$\begin{aligned} \partial_t^2 \Psi &= v^2\gamma^2\delta'(x - vt) \cos \vartheta + \gamma^4[2v + v^3 + v^2\text{sgn}(x - vt)]\delta(x - vt) \sin \vartheta \\ &\quad - \frac{1}{2}\gamma^6[3v + v^3 + (3v^2 + 1)\text{sgn}(x - vt)] \cos \vartheta, \end{aligned} \quad (\text{B12})$$

and then likewise compute

$$\partial_x \Psi = \gamma^2 \delta(x - vt) \cos \vartheta + \frac{1}{2}\gamma^4[1 + v^2 + 2v\text{sgn}(x - vt)] \sin \vartheta \quad (\text{B13})$$

$$\begin{aligned} \partial_x^2 \Psi &= \gamma^2\delta'(x - vt) \cos \vartheta + \gamma^4[3v + \text{sgn}(x - vt)]\delta(x - vt) \sin \vartheta \\ &\quad - \frac{1}{2}\gamma^6[3v + v^3 + (3v^2 + 1)\text{sgn}(x - vt)] \cos \vartheta. \end{aligned} \quad (\text{B14})$$

Combination of Eqs. (B11) and (B13) yields

$$-\partial_t^2 \Psi + \partial_x^2 \Psi = \delta'(x - vt) \cos \vartheta + \gamma^2[v + \text{sgn}(x - vt)]\delta(x - vt) \sin \vartheta. \quad (\text{B15})$$

By the selection properties of $\delta'(u)$, we have

$$\delta'(x - vt) \cos \vartheta = \delta'(x - vt) \cos t - \gamma^2[v + \text{sgn}(x - vt)]\delta(x - vt) \sin t. \quad (\text{B16})$$

Substituting this result into (B15), using the selection property of $\delta(u)$, and realizing that $\delta(u) \text{sgn } u = 0$ by symmetry, we arrive at the desired result, $-\partial_t^2 \Psi + \partial_x^2 \Psi = \delta'(x - vt) \cos t$.

APPENDIX C: SOURCE TERMS

This appendix lists the specific functions $F_{\ell m}(t, r)$ and $G_{\ell m}(t, r)$ for our polar and axial cases. However, one practical difference between the functions listed below, and what we have used in our numerical simulations is the following. In accordance with our unphysical choice of vanishing initial data, we “switch on” the source terms smoothly via the following prescription:

$$F_{\ell m}(t, r) \rightarrow \begin{cases} \frac{1}{2}[\text{erf}(\sqrt{\delta}(t - t_0 - \tau/2) + 1)]F_{\ell m}(t, r) & \text{for } t_0 \leq t \leq t_0 + \tau \\ F_{\ell m}(t, r) & \text{for } t > t_0 + \tau, \end{cases} \quad (\text{C1})$$

and the same for $G_{\ell m}(t, r)$. Typically, the initial time $t_0 = 0$, and the timescale τ is much shorter than the final time of the run. Choosing suitable τ and δ , we ensure that our start-up is smooth to machine precision, and thereby avoid the troublesome nature of an impulsively started problem. Note that this prescription does initially affect the form of $\partial_t F_{\ell m}(t, r)$.

To both express and derive concrete expressions for the source terms, we rely on standard results for particle motion in the Schwarzschild geometry [10, 17]. As an alternative set to (e, p) discussed in Section II A, we may instead work with (E_p, L_p) , the physical particle energy and angular

momentum (both per unit mass). These constants of the motion are related to our original set by [18, 19]

$$L_p^2 = \frac{p^2 M^2}{p - 3 - e^2}, \quad E_p^2 = \frac{(p - 2)^2 - 4e^2}{p(p - 3 - e^2)}. \quad (\text{C2})$$

Let $z^\mu(\tau) = (t(\tau), r(\tau), \theta(\tau), \phi(\tau))$ be the parameterization of the particle's four-trajectory in terms of proper time τ . As before, set $r_p(t) = r(\tau(t))$ for the radial coordinate of the particle expressed in terms of coordinate time, with similar expressions for $\theta_p(t)$ and $\phi_p(t)$. We assume that the coordinate system has been selected to ensure equatorial motion, $\theta_p(t) = \pi/2$. Then the four-velocity $u^\mu = dz^\mu/d\tau$ has components

$$u^t = E_p/f(r), \quad (u^r)^2 = E_p^2 - f(r)(1 + L_p^2/r^2), \quad u^\theta = 0, \quad u^\phi = L_p/r^2, \quad (\text{C3})$$

where these expressions follow from standard conservation arguments [10, 17].

Throughout this appendix, we use m_p for the particle mass in order to avoid confusion with the azimuthal spherical harmonic index m .

1. Zerilli–Moncrief (polar) source term

To define the Zerilli–Moncrief source term, we first introduce the polar spherical harmonics

$$Y^{\ell m}, \quad Y_a^{\ell m} = Y_{:a}^{\ell m}, \quad Y_{ab}^{\ell m} = Y^{\ell m} \gamma_{ab}, \quad Z_{ab}^{\ell m} = Y_{:ab}^{\ell m} + \frac{\ell(\ell+1)}{2} Y^{\ell m} \gamma_{ab}, \quad (\text{C4})$$

where $Y^{\ell m}(\theta, \phi)$ are the ordinary scalar harmonics [34], γ_{ab} is the metric of the unit-radius round sphere, and a colon indicates covariant differentiation compatible with γ_{ab} . The Zerilli–Moncrief source term is specified by⁴

$$f(r) F_{\ell m}^{\text{ZM}}(t, r) = e_\ell(r) \bar{Y}^{\ell m}(t) \quad (\text{C5a})$$

$$f(r) G_{\ell m}^{\text{ZM}}(t, r) = a_\ell(r) \bar{Y}^{\ell m}(t) + b_\ell(r) \bar{Y}_\phi^{\ell m}(t) + c_\ell(r) \bar{Y}_{\phi\phi}^{\ell m}(t) + d_\ell(r) \bar{Z}_{\phi\phi}^{\ell m}(t). \quad (\text{C5b})$$

Here, for example, $\bar{Y}^{\ell m}(t) \equiv \bar{Y}^{\ell m}(\pi/2, \phi_p(t))$. Moreover, the coefficients in (C5) are given by [9, 18]

$$a_\ell(r) = \frac{8\pi m_p}{(1 + n_\ell)} \frac{f^2(r)}{r \Lambda_\ell^2(r)} \left\{ \frac{6ME_p}{r} - \frac{\Lambda_\ell(r)}{E_p} \left[1 + n_\ell - \frac{3M}{r} + \frac{L_p^2}{r^2} \left(n_\ell + 3 - \frac{7M}{r} \right) \right] \right\} \quad (\text{C6a})$$

$$b_\ell(r) = \frac{16\pi m_p}{(1 + n_\ell)} \frac{f^2(r)}{r^2 \Lambda_\ell(r)} \frac{L_p}{E_p} u^r \quad (\text{C6b})$$

$$c_\ell(r) = \frac{8\pi m_p}{(1 + n_\ell)} \frac{f^3(r)}{r^3 \Lambda_\ell(r)} \frac{L_p^2}{E_p} \quad (\text{C6c})$$

$$d_\ell(r) = -32\pi m_p \frac{(\ell - 2)!}{(\ell + 2)!} \frac{f^2(r)}{r^3} \frac{L_p^2}{E_p} \quad (\text{C6d})$$

$$e_\ell(r) = \frac{8\pi m_p}{(1 + n_\ell)} \frac{f^3(r)}{\Lambda_\ell(r)} \frac{1}{E_p} \left(1 + \frac{L_p^2}{r^2} \right), \quad (\text{C6e})$$

where $n_\ell = (\ell + 2)(\ell - 1)/2 = \Lambda_\ell(r) - 3M/r$, and u^r is determined by (C3) and the sign of $\dot{r}_p(t)$. Due to the u^r factor, we may not, strictly speaking, interpret $b_\ell(r)$ as solely a function of r , but $f(r)u^r/E_p$ could also be reinterpreted as $\dot{r}_p(t)$ and paired with $\bar{Y}_\phi^{\ell m}(t)$.

⁴ Factors of $f(r)$ are included here in order to have direct comparison with the same coefficients listed in Refs. [9, 18].

2. Cunningham–Price–Moncrief (axial) source term

With ϵ_{ab} the unit-sphere Levi-Civita tensor such that $\epsilon_{\theta\phi} = -\sin\theta$, the axial spherical harmonics are

$$S_a^{\ell m} = \gamma^{bc} \epsilon_{ab} Y_{:c}^{\ell m}, \quad S_{ab}^{\ell m} = S_{(a:b)}^{\ell m}, \quad (\text{C7})$$

and we express the Cunningham–Price–Moncrief source term as

$$f(r) F_{\ell m}^{\text{CPM}}(t, r) = C_\ell(r) \bar{S}_\phi^{\ell m}(t) \quad (\text{C8a})$$

$$f(r) G_{\ell m}^{\text{CPM}}(t, r) = A_\ell(r) \bar{S}_\phi^{\ell m}(t) + B_\ell(r) \bar{S}_{\phi\phi}^{\ell m}(t). \quad (\text{C8b})$$

As before, (t) indicates evaluation on $(\theta, \phi) = (\pi/2, \phi_p(t))$, and the coefficients in the above expressions are as follows:

$$A_\ell(r) = 32\pi m_p \frac{(\ell-2)!}{(\ell+2)!} \frac{f^2(r)}{r^2} \frac{L_p}{E_p^2} \left[f(r) - 2E_p^2 - \left(1 - \frac{5M}{r}\right) \left(1 + \frac{L_p^2}{r^2}\right) \right] \quad (\text{C9a})$$

$$B_\ell(r) = 32\pi m_p \frac{(\ell-2)!}{(\ell+2)!} \frac{f^2(r)}{r^3} \frac{L_p^2}{E_p^2} u^r \quad (\text{C9b})$$

$$C_\ell(r) = 32\pi m_p \frac{(\ell-2)!}{(\ell+2)!} \frac{f^3(r)}{r} \frac{L_p}{E_p^2} \left(1 + \frac{L_p^2}{r^2}\right). \quad (\text{C9c})$$

As before, we may not truly interpret $B_\ell(r)$ as a function of r , but nevertheless keep this convenient notation. We note that our $A_\ell(r)$ does not agree with the corresponding factor $u_\ell(r)$ quoted in Ref. [9]; however, we find that $u_\ell(r) = A_\ell(r) - C'_\ell(r)$. Due to this discrepancy, we present our derivation of (C9).

3. Derivation of the axial source term

Our goal is to establish formulas (C8,C9) for the Cunningham–Price–Moncrief source term,

$$S^{\text{CPM}} = G^{\text{CPM}} \delta(r - r_p(t)) + F^{\text{CPM}} \delta'(r - r_p(t)). \quad (\text{C10})$$

Here and in what follows, we suppress (ℓ, m) indices wherever possible. Our starting point is Martel and Poisson's expression for S^{CPM} in (t, r) coordinates,

$$S^{\text{CPM}} = \frac{2r}{(\ell-1)(\ell+2)} \left(f^{-1} \partial_t P^r + f \partial_r P^t + \frac{2M}{r^2} P^t \right). \quad (\text{C11})$$

This result appears in Appendix C of their expanded version of [8], where S_{odd} in that reference is our S^{CPM} . The vector $P^A = (P^t, P^r)$ is given by Eq. (5.10) of [8],

$$P^A = \frac{16\pi r^2}{\ell(\ell+1)} \int_{S^2} d\Omega T^{Ab} \bar{S}_b^{\ell m}, \quad (\text{C12})$$

but here with our index conventions and harmonics. Note that $S_a^{\ell m}$ corresponds to $X_A^{\ell m}$ of [8].

The stress-energy tensor for a point particle is

$$T^{\mu\nu} = m_p \int d\tau (-g)^{-1/2} u^\mu u^\nu \delta^4(x - z(\tau)), \quad (\text{C13})$$

here with $g = -r^4 \sin^2 \theta$ the determinant of the background Schwarzschild metric (4). We now change coordinates $d\tau = (d\tau/dt)dt$, integrate over t , and use $u^t = dt/d\tau$, thereby finding

$$T^{\mu\nu} = m_p \frac{u^\mu u^\nu}{u^t r^2 \sin \theta} \delta(r - r_p(t)) \delta(\theta - \theta_p(t)) \delta(\phi - \phi_p(t)). \quad (\text{C14})$$

Combination of Eqs. (C12) and (C14), with the assumption of equatorial motion, then gives

$$P^A = \frac{16\pi m_p}{\ell(\ell+1)} \frac{u^A u^\phi}{u^t} \bar{S}_\phi(\pi/2, \phi_p(t)) \delta(r - r_p(t)), \quad (\text{C15})$$

Because we have not integrated over r , the four-velocity components u^μ here may be viewed either as functions solely of r , or solely of t upon replacing r by $r_p(t)$. Either viewpoint will yield the same derivatives $\partial_B P^A$ insofar as integration against test functions is concerned, and we view the components u^μ as depending on r . The delta functions of course depend on both r and t . Having identified which terms depend on r and t , we then calculate

$$\partial_r P^t = \frac{16\pi m_p}{\ell(\ell+1)} (\partial_r u^\phi) \bar{S}_\phi \delta(r - r_p(t)) + \frac{16\pi m_p}{\ell(\ell+1)} u^\phi \bar{S}_\phi \partial_r \delta(r - r_p(t)) \quad (\text{C16})$$

$$\partial_t P^r = \frac{16\pi m_p}{\ell(\ell+1)} \frac{u^r u^\phi}{u^t} \left\{ \left[\frac{u^\phi}{u^t} (\partial_\phi \bar{S}_\phi) - \partial_r \left(\frac{u^r}{u^t} \right) \bar{S}_\phi \right] \delta(r - r_p(t)) - \frac{u^r}{u^t} \bar{S}_\phi \partial_r \delta(r - r_p(t)) \right\}. \quad (\text{C17})$$

To reach the last equation, we have replaced $\dot{\phi}_p(t)$ by u^ϕ/u^t , which is permissible due to the presence of the accompanying delta function. Moreover, we have also made the replacement

$$\dot{r}_p(t) \delta'(r - r_p(t)) \rightarrow \frac{u^r}{u^t} \delta'(r - r_p(t)) + \left(\frac{u^r}{u^t} \right)' \delta(r - r_p(t)), \quad (\text{C18})$$

where the prime denotes partial r -differentiation. Finally, substitution of the last two results into Eq. (C11), along with Eq. (C3) and the identity

$$\partial_r \left(\frac{u^r}{u^t} \right)^2 = \frac{2}{E_p^2} \frac{f^2(r)}{r} \left[\left(1 - \frac{5M}{r} \right) \left(1 + \frac{L_p^2}{r^2} \right) - f(r) \right] + \frac{4Mf(r)}{r^2}, \quad (\text{C19})$$

yields the desired results (C8,C9). We have also used $S_{\phi\phi}(\pi/2, \phi) = \partial_\phi S_\phi(\pi/2, \phi)$, that is ordinary partial differentiation suffices in the equatorial plane.

-
- [1] Current website for the project: lisa.nasa.gov, December 2008.
 - [2] S. A. Hughes, *Lisa sources and science*, Proceedings of the 7th Edoardo Amaldi Conference on Gravitational Waves, [arXiv:0711.0188](https://arxiv.org/abs/0711.0188) (2007).
 - [3] E. Poisson, *The Motion of Point Particles in Curved Spacetime*, Living Rev. Relativity 7 (2004) 6 (136 pages). Available at www.livingreviews.org/lrr-2004-6.
 - [4] P. A. Sundararajan, G. Khanna, and S. A. Hughes, *Towards Adiabatic Waveforms for Inspiral into Kerr Black Holes: A New Model of the Source for the Time Domain Perturbation Equation*, Phys. Rev. D, 74 (2007) 104005 (20 pages). Expanded version available as [arXiv:gr-qc/0703028v3](https://arxiv.org/abs/gr-qc/0703028v3).
 - [5] L. Barack and C. Cutler, *LISA capture sources: Approximate waveforms, signal-to-noise ratios, and parameter estimation accuracy*, Phys. Rev. D, 69 (2004) 082005 (24 pages).
 - [6] T. Regge and J. Wheeler, *Stability of a Schwarzschild Singularity*, Phys. Rev. 108 (1957) 1063-1069.
 - [7] F. J. Zerilli, *Effective Potential for Even-Parity Regge-Wheeler Gravitational Perturbation Equations*, Phys. Rev. Lett., 24 (1970) 737-738.

- [8] K. Martel and E. Poisson, *Gravitational perturbations of the Schwarzschild spacetime: A practical covariant and gauge-invariant formalism*, Phys. Rev. D, 71 (2005) 104003 (13 pages). Expanded version available as [arXiv:gr-qc/0502028](#).
- [9] C. F. Sopuerta and P. Laguna, *Finite element computation of the gravitational radiation emitted by a pointlike object orbiting a nonrotating black hole*, Phys. Rev. D, 73 (2006) 044028 (17 pages).
- [10] C. W. Misner, K. S. Thorne, and J. A. Wheeler, *Gravitation* (Freeman, New York, 1973).
- [11] C. O. Lousto, *A time-domain fourth-order-convergent numerical algorithm to integrate black hole perturbations in the extreme-mass-ratio limit*, Class. Quantum Grav. 22 (2005) S543-S568.
- [12] J.-H. Jung, G. Khanna, and I. Nagle, *A spectral collocation approximation of one-dimensional head-on collisions of black-holes*, to appear in Int. J. Mod. Phys. C, 19 pages, [arXiv:0711.2545](#) (2007).
- [13] P. Cañizares and C. F. Sopuerta, *Simulations of Extreme-Mass-Ratio Inspirals Using Pseudospectral Methods*, J. Phys. Conf. Series 154 (2009) 012053 (6 pages), [arXiv:0811.0294](#).
- [14] J. S. Hesthaven and T. Warburton, *High-Order Accurate Methods for Time-domain Electromagnetics*, Comp. Mod. Engin. Sci. 5 (2004) 395-408.
- [15] J. S. Hesthaven and T. Warburton, *Nodal Discontinuous Galerkin Methods: Algorithms, Analysis, and Applications* (Springer-Verlag, New York, 2008).
- [16] G. Zumbusch, *Finite Element, Discontinuous Galerkin, and Finite Difference evolution schemes in spacetime*, 15 pages, [arXiv:0901.0851](#) (2009).
- [17] S. Chandrasekhar, *The Mathematical Theory of Black Holes* (Oxford University Press, Oxford, 2000).
- [18] K. Martel, *Gravitational waveforms from a point particle orbiting a Schwarzschild black hole*, Phys. Rev. D, 69 (2004) 044025 (20 pages).
- [19] C. Cutler, D. Kennefick, and E. Poisson, *Gravitational radiation reaction for bound motion around a Schwarzschild black hole*, Phys. Rev. D, 50 (1994), 3816-3835.
- [20] M. H. Carpenter and C. Kennedy, *Fourth Order 2N-Storage Runge-Kutta Schemes*, NASA Technical Memorandum 109112 (1994).
- [21] K. Fan, W. Cai, X. Ji, *A generalized discontinuous Galerkin (GDG) method for Schrödinger equations with nonsmooth solutions*, J. Comp. Phys., 227 (2008) 2387-2410.
- [22] S. R. Lau, *Analytic structure of radiation boundary kernels for blackhole perturbations*, J. Math. Phys., 46 (2005) 102503 (21 pages).
- [23] B. Alpert, L. Greengard, and T. Hagstrom, *Rapid Evaluation of Nonreflecting Boundary Kernels for Time-Domain Wave Propagation*, SIAM J. Numer. Anal., 37 (2000) 1138-1164.
- [24] E. Poisson, *Gravitational radiation from a particle in circular orbit around a black hole. I. Analytical results for the nonrotating case*, Phys. Rev. D, 47 (1993) 1497-1510.
- [25] M. Davis, R. Ruffini, W. H. Press, and R. H. Price, *Gravitational Radiation from a Particle Falling Radially into a Schwarzschild Black Hole*, Phys. Rev. Lett. 27 (1971) 1466-1469.
- [26] A. M. Abrahams and C. R. Evans, *Reading off gravitational radiation waveforms in numerical relativity calculations: Matching to linearized gravity*, Phys. Rev. D, 37 (1988) 318-332.
- [27] A. M. Abrahams and C. R. Evans, *Gauge-invariant treatment of gravitational radiation near the source: Analysis and numerical simulations*, Phys. Rev. D, 42 (1990) 2585-2594.
- [28] T. Tanaka, M. Shibata, M. Sasaki, H. Tagoshi, and T. Nakamura, *Gravitational Wave Induced by a Particle Orbiting around a Schwarzschild Black Hole*, Prog. Theo. Phys. 90 (1993) 65-83.
- [29] L. Barack, Y. Mino, H. Nakano, A. Ori, and M. Sasaki, *Calculating the Gravitational Self-Force in Schwarzschild Spacetime*, Phys. Rev. Lett. 88 (2002) 091101 (4 pages).
- [30] L. Barack and N. Sago, *Gravitational self-force on a particle in circular orbit around a Schwarzschild black hole*, Phys. Rev. D, 75 (2007) 064021 (25 pages).
- [31] S. Detweiler, *Consequence of the gravitational self-force for circular orbits of the Schwarzschild geometry*, Phys. Rev. D, 77 (2008) 124026 (15 pages).
- [32] A. Nagar, T. Damour, and A. Tartaglia, *Binary black hole merger in the extreme mass ratio limit*, Class. Quant. Grav. 24 (2007) S109-S124.
- [33] N. Sago, L. Barack, S. Detweiler, *Two approaches for the gravitational self-force in black hole spacetime: Comparison of numerical results*, Phys. Rev. D, 78 (2008) 124024 (9 pages).
- [34] K. S. Thorne, *Multipole expansions of gravitational radiation*, Rev. Mod. Phys. 52 (1980) 299-339.